Frictional State Evolution During Normal Stress Perturbations Probed With Ultrasonic Waves

Srisharan Shreedharan[1,2] , **Jacques Rivière[2,3]** , **Pathikrit Bhattacharya[4,5]** , and **Chris Marone[1,2]**

[1]Department of Geosciences, Pennsylvania State University, University Park, PA, USA, [2]G3 Center for Geomechanics, Geofluids and Geohazards, University Park, PA, USA, [3]Department of Engineering Science and Mechanics, Pennsylvania State University, University Park, PA, USA, [4]Now at School of Earth, Ocean and Climate Sciences, IIT Bhubaneswar, Argul, India, [5]Department of Civil and Environmental Engineering, Tufts University, Medford, MA, USA

Abstract Fault normal stress changes dynamically during earthquake rupture; however, the impact of these changes on dynamic frictional strength is poorly understood. Here we report on a laboratory study to investigate the effect of normal stress perturbations on the friction of westerly granite surfaces sheared under normal stresses of 1-25 MPa. We measure changes in surface friction and elastic properties, using acoustic waves, for step changes in normal stress of 1–50% and shearing velocities of 1-100 μm/s. We demonstrate that transmitted elastic wave amplitude is a reliable proxy for the real contact area at the fault interface at steady state. For step increases in normal stress, wave amplitude increases immediately and then continues to increase during elastic shear loading to a peak value from which it decreases as fault slip rate increases. Friction changes in a similar fashion, showing an inelastic increase over a characteristic shear displacement that is independent of loading rate. Perturbations in normal stress during shear cause excursions in the frictional slip rate that must be accounted for in order to accurately predict the evolution of fault strength and elastic properties. Our work improves understanding of induced seismicity and triggered earthquakes with particular focus on simulating static triggering and stress transfer phenomena using rate-and-state frictional formulations in earthquake rupture models.

1. Introduction

Changes in fault normal stress occur commonly and play a key role in determining shear stability and frictional properties of tectonic faults. For example, both static changes in stress state around a fault and dynamic stressing associated with passing seismic waves can trigger seismicity and cause catastrophic earthquake failure. Moreover, observations immediately following the 1992 M_w 7.3 Landers earthquake showed that aftershocks tended to occur primarily in regions of reduced normal stress (Harris, 1998; Harris & Simpson, 1992) and changes in the regional stress state immediately following fault slip have been robustly linked to seismicity on nearby faults, sometimes within hours or days of the mainshock (Freed, 2005; King et al., 1994). Also, passing seismic waves due to moderate and large earthquakes have been known to cause seismicity due to dynamic stress changes both in the near field and in the far field (Fan & Shearer, 2016; Gomberg & Johnson, 2005; Hill et al., 1993; Johnson et al., 2015; Kilb et al., 2000). In addition to conventional seismicity, deep tectonic tremor (Peng & Gomberg, 2010; Rubinstein et al., 2008) and slow slip events (Itaba & Ando, 2011; Wallace et al., 2017) have also been causally linked to changes in stress and/or frictional strength via dynamic stressing by near-field and teleseismic earthquakes.

Changes in fault stress state have also been implicated for induced seismicity associated with wastewater injection, energy production, and other anthropogenic activities (e.g., Goebel & Brodsky, 2018; Gomberg et al., 1998; Raleigh et al., 1976; Van der Elst et al., 2013). Earthquake triggering by ocean tides and seismic triggering of volcanic activity are also examples of the importance of understanding how frictional state evolves during perturbations in normal stress (e.g., Delorey et al., 2017; Manga & Brodsky, 2006; Tan et al., 2018; Tanaka et al., 2006).

Quantifying how changes in normal stress impact faulting is also important in the context of geometric complexities and material heterogeneities along tectonic faults. Observations of fault traces by Wesnousky (2006) and dynamic rupture models by Bhat et al. (2004) and Dunham et al. (2011) show that stress concentrations at bends or stepovers may reduce or enhance the possibility of fault rupture. Dynamic rupture simulations
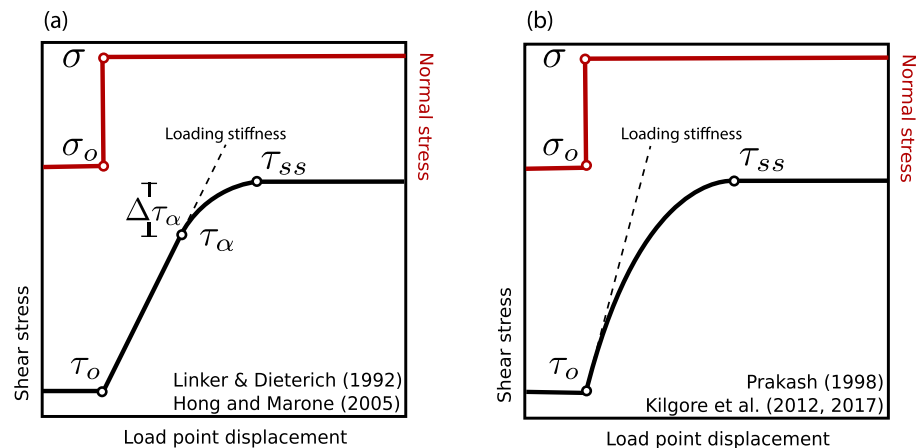
Figure 1. Two contrasting models for shear stress evolution after a step increase in normal stress from σ_0 to σ. $\Delta\tau_\alpha$ is the nonlinear shear strength increase associated with frictional state evolution. (a) Shear stress increases linearly until a critical value τ_α, after which it increases nonlinearly to a new steady state value corresponding to σ. (b) Shear stress evolves nonlinearly until a new steady state value is attained; the fault never locks and the shear stress evolution curve has a slope smaller than the loading stiffness.

on bimaterial faults have shown the development of normal stress variations giving rise to rupture directivity (Andrews & Ben-Zion, 1997; Ma & Beroza, 2008).

Broadly, two classes of frictional responses have been proposed in response to changes in normal stress during steady frictional sliding (Figure 1). One model is a three-stage response (Figure 1a) in which a sudden increase in normal stress first causes an instantaneous shear stress increase due to Poisson coupling of normal and shear stresses, then a linear increase in shear stress followed by a quasi-exponential increase to a new steady state frictional strength (Hobbs & Brady, 1985; Linker & Dieterich, 1992; Olsson, 1988). Another model suggests a single-stage response in which shear stress grows exponentially with slip or time (Figure 1b) without a linear elastic stage (Prakash, 1998; Prakash & Clifton, 1993).

Linker and Dieterich (1992) proposed an explanation for the first model based on a linear strength increase followed by slip-dependent evolution upon a step change in normal stress (Figure 1a). They introduced an empirical constant α in the rate-and-state frictional (RSF) formulation to account for evolution of the real area of contact (Dieterich, 1979; Marone, 1998a; Ruina, 1983). Subsequent work on bare granite surfaces, quartz, and clay/quartz gouge confirmed the three-stage frictional response (Boettcher & Marone, 2004; Hong & Marone, 2005; Richardson & Marone, 1999). Linker and Dieterich (1992) attributed the first stage, which involves a small shear stress increase in response to a normal stress step (NSS) increase, to the elastic Poisson effect and perhaps slight misalignment in their biaxial load frame. The subsequent works reported only a very small first stage, followed by a linear-elastic stress increase and the inelastic response associated with the parameter α.

In contrast, results from plate impact experiments on metals indicate that shear stress may evolve in a single, nonlinear mode (Figure 1b) following a sudden change in normal stress (Prakash, 1998; Prakash & Clifton, 1993). This interpretation is also favored by recent works that report a single-stage increase in shear stress after abrupt, small changes in fault normal stress (Bhattacharya, 2017; Kilgore et al., 2012, 2017).

The two classes of friction response to a normal stress perturbation (Figure 1) result in conflicting interpretations of the microscale contact physics. The Linker and Dieterich (1992) style of shear stress evolution (Figure 1a) implies that the fault slip rate reduces sufficiently to effectively lock the fault interface. For this to occur, an increase in normal stress should be accompanied by an increase in contact area with the newly created contacts having a shear resistance comparable to that of existing contacts. On the other hand, Kilgore et al. (2012) argued, based on their observation of a lack of this behavior, that the new contacts have near-zero inherent strength and that either slip or time is required for strength increase. Kilgore et al. (2017) suggested a finite slip rate excursion across the NSS, which implies a finite and nonzero shear resistance at the contact scale. Despite this, their experiments exhibit a slower and apparently slip (or time) dependent

increase in shear stress even though contact area inferred indirectly via ultrasonic monitoring and fault dilation shows a rapid increase across the NSS. Based on this, they argue for a contrast in shear resistance between the pre-NSS and post-NSS contacts and suggest an exponential model for shear stress evolution, which ensures numerical stability across the NSS (Cochard & Rice, 2000; Ranjith & Rice, 2001).

The purpose of this study is to illuminate the contact mechanics and frictional processes that accompany perturbations in fault normal stress. We report on a detailed experimental investigation designed to understand the contact processes that dictate friction and resolve the discrepancies between the two models summarized in Figure 1. Our study includes continuous ultrasonic monitoring of the fault surface and a range of conditions spanning those of previous works (Boettcher & Marone, 2004; Hong & Marone, 2005; Kilgore et al., 2012, 2017; Linker & Dieterich, 1992; Nagata et al., 2008, 2012, 2014; Richardson & Marone, 1999). A caveat of all previous laboratory studies on normal stress perturbations is the assumption of a single, constant value of loading stiffness and that changes in slip rate associated with a change in normal stress can be ignored for the range of conditions explored. However, recent work demonstrates that changing normal stress has a nontrivial effect on loading stiffness (Leeman et al., 2015, 2016, 2018; Scuderi et al., 2016, 2017). Here we measure the effect of normal stress on shear loading stiffnesses and account for it in our data analyses and numerical simulations. We show that shear stress evolution follows the three-step response of Figure 1a for the normal stress and velocity histories explored by previous works. Our results indicate that the contrasting results of previous works can be resolved by invoking a combination of slip and time-dependent friction evolution, by considering the effect of normal stress on loading stiffness, and through a careful consideration of the slip rate excursion across the NSSs. We also find that transmitted elastic wave amplitude provides a feasible proxy for steady state real contact area in bare granite frictional interfaces over the range of normal stresses, velocities, and shear strains explored in our study.

2. Experimental Methods

The experiments reported in this study were performed on a biaxial testing apparatus in a double direct-shear (DDS) configuration (Marone, 1998b; Rivière et al., 2018; Scuderi et al., 2014). Shear experiments were performed on bare westerly granite surfaces ground to 60-grit roughness prior to each experiment to ensure reproducibility. The friction surfaces were measured to be flat and parallel to within 25 μm over the 10-cm $\times$ 10-cm nominal contact area. The biaxial loading apparatus consists of two hydraulic rams that apply normal and shear loads on the friction surfaces (Figure 2). Our machine is fully servo-controlled and can operate in either displacement or load control. A strain-gauge load cell and direct current differential transformer are mounted on each loading ram (Figure 2). Load cells are calibrated with a Morehouse proving-ring and are accurate to $\pm$5 N; direct current differential transformers are calibrated with a Vernier height gauge and are accurate to $\pm$0.1 μm. We used broadband (~0.02–2 MHz) P wave lead-zirconate (PZT) ultrasonic acoustic transducers (Boston Piezo-Optics Inc. PZT-5A 0.5″ diameter compressional crystals) to monitor the friction surfaces during shear. The PZTs were embedded in steel loading platens of the same height and width as the granite side blocks of the DDS configuration (Figure 2b) and the surfaces between the steel platens and granite blocks were covered with a film of molasses before each experiment. Experiments were conducted at room temperature and over a range of relative humidity (RH) from <10 to 100% RH (Table 1). Mechanical data were logged using a 24-bit $\pm$10 V analog to digital converter at a sampling rate of 10 kHz and averaged in real time to obtain a sampling rate of 100 or 1,000 Hz. Ultrasonic acoustic pulses were sampled at 25 MHz using a Verasonics ultrasonic data acquisition system with a pulse rate of 0.1-1 kHz.

2.1. Sample configuration

Three westerly granite blocks were used in the DDS configuration (Figure 2). Each of the four friction surfaces were roughened by polishing with a small granite flat and #60 grit silicon carbide grains and water. Westerly granite was used for its fine-grained nature, the extensive literature on it (Biegel et al., 1992; Byerlee, 1967; Haimson & Chang, 2000; Solberg & Byerlee, 1984; Tullis & Yund, 1977; Wong, 1982), and to facilitate direct comparison between our results and previous works on frictional state evolution (Hong & Marone, 2005; Kilgore et al., 2017; Linker & Dieterich, 1992). We used two sets of westerly granite blocks, one with nominal contact area of 10 cm $\times$ 10 cm and another with nominal contact area of 5 cm $\times$ 5 cm (Figure 2). The fault surfaces were buttressed by machining a recess (2 mm wide and 1 mm deep) along each edge, such that the nominal frictional contact dimensions were slightly smaller than the block dimensions.
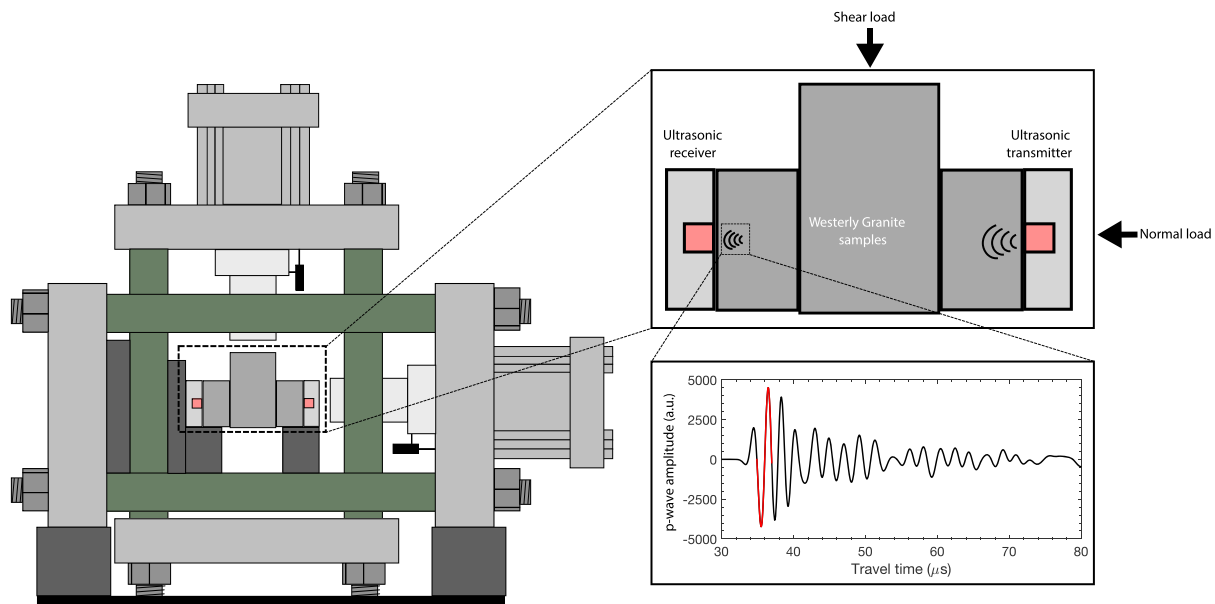
Figure 2. Schematic of the testing machine and sample assembly for double direct shear friction experiments. Displacement transducers (black rectangles) measure the position of the loadpoint for fault normal and shear loading. Ultrasonic pulses are transmitted and recorded by lead-zirconate (PZT) transducers (pink squares) embedded in steel loading platens adjacent to the sample. Lower inset shows representative waveform; red portion indicates the segment used for all ultrasonic analyses reported in this study.

2.2. Experimental Procedure

We conducted two types of experiments to probe frictional state evolution during normal stress perturbations. The first set (Figure 3) involved NSS experiments similar to previous works (Hong & Marone, 2005; Kilgore et al., 2012, 2017;Linker & Dieterich, 1992 ; Richardson & Marone, 1999). These were performed with a computer controlled NSS history and constant shear loadpoint velocity. Normal stress was increased rapidly to create "steps" of 1-50% increase from a nominal baseline value of 2-12 MPa. We tuned the servo controller such that the step change occurred in <0.2 s with minimal overshoot, which ensures that measured variations in shear stress are solely the result of the NSS with minimal overprinting by stress vibrations. Despite this, we observe a small increase in shear stress, which we attribute to the Poisson effect for constant shear loading rate (Linker & Dieterich, 1992; Richardson & Marone, 1999). For a given experiment we imposed up to 14 stress steps and our suite of experiments explored a range of shear velocities from 1 to 60 µm/s (Table 1).

Our second set of experiments (Figure 4) was designed to measure loading stiffness for the range of conditions explored in our NSS tests. These runs used the same DDS sample configuration (Table 1). We imposed shear load/unload sequences at constant normal stress and measured the loading stiffness from the slope of the linear portion of the reload curves (Leeman et al., 2015). This procedure was repeated for each normal stress in increments of 0.5 MPa from 2 to 22 MPa (Figure 4).

All experiments were conducted at room temperature and humidity except those conducted at 100% RH for which the samples were enclosed in a flexible humidity-controlled membrane (Table 1). The humidity state was maintained by continuously supplying the enclosed system with a mist of water vapor using a humidifier (Frye

Table 1
List of Experiments and Associated Boundary Conditions

Experiment	Type	Baseline normal stress (MPa)	Sliding rate (µm/s)	Relative humidity (%)
p4819	NSS	8	4, 21	27.1
p4861	NSS	8	11, 21, 42, 64	39
p4862	NSS	4	11, 21, 42, 64	46.6
p4863	NSS	2	11, 21, 42, 64	46.6
p4864	NSS	10	11, 21, 42, 64	48
p4908	NSS	8	11, 21	74
p4909	NSS	8	11, 21, 42, 64	63
p4919	S	0.5-12	11	76
p5006	NSS	12	1.29, 11, 64	100
p5007	NSS	12	1.29, 11, 64	100
p5008	NSS	4	1.29, 11, 64	100
p5009	NSS	4	1.29, 11, 64	100
p5010	S	0.5–25	11	100
p5011	S	0.5–25	11	100
p5012	S	0.5–25	11	100
p5013	S	0.5–25	11	100
p5023	NSS	12	1.29, 64	16.3
p5024	NSS	12	1.29, 64	100
p5025	NSS	12	1.29, 64	100

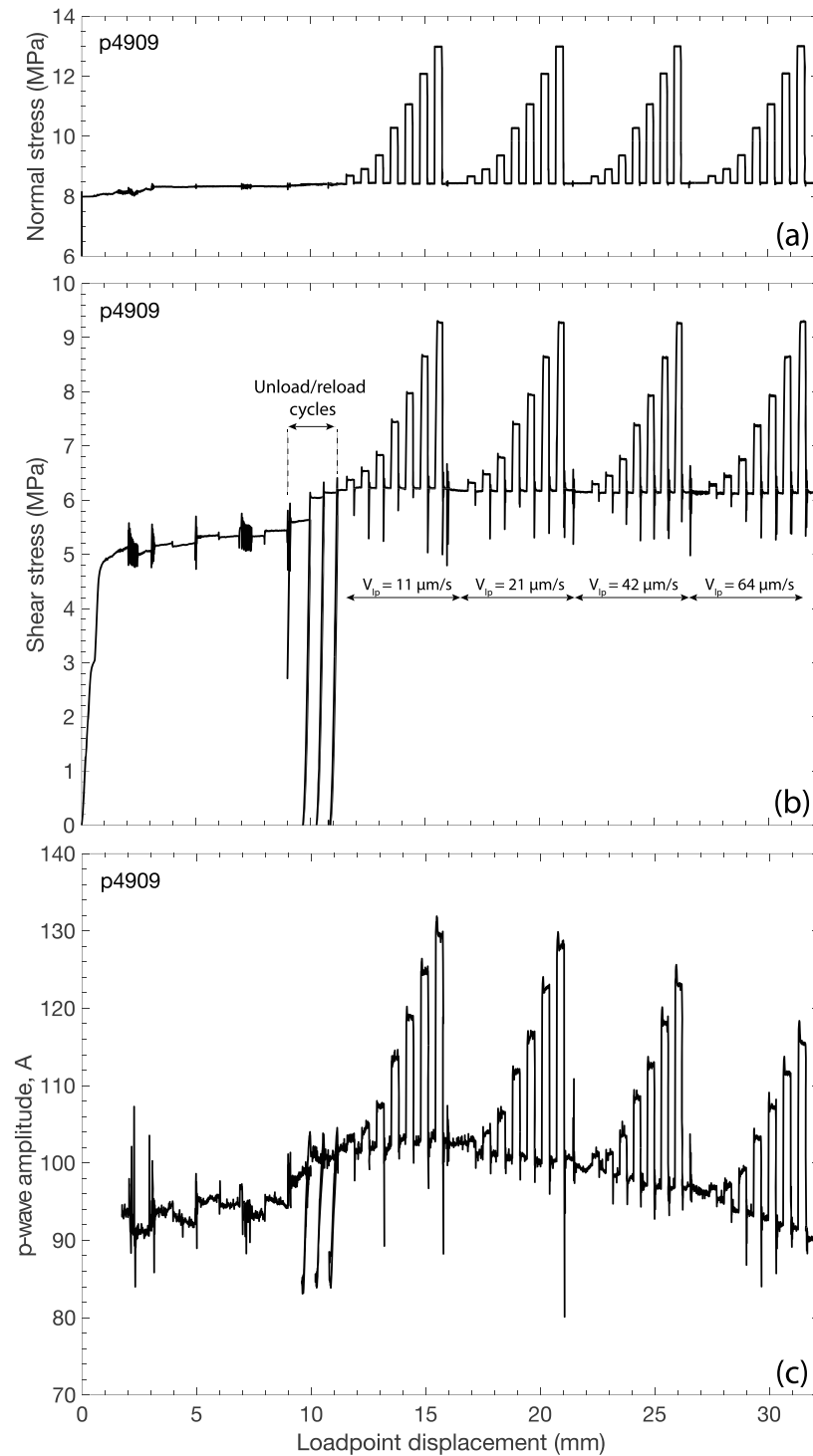Abbreviations: NSS, normal stress step; S, stiffness.

Figure 3. Results from a typical experiment showing four normal stress step sequences. (a) Imposed normal stress history. (b) Shear stress response. (c) Peak-to-peak amplitude of the ultrasonic waveforms (see Figure 2 inset). Experiments consist of multiple sequences of normal stress steps (1–50% increases from a baseline value).

& Marone, 2002). For our NSS experiments (Figure 3), a constant shear displacement rate was imposed until the shear stress attained a steady state value and a total slip of 5 mm was accumulated on the fault surfaces. We report coefficient of friction as the ratio of shear stress to normal stress on the fault plane and assume that each fault of the DDS arrangement is identical.
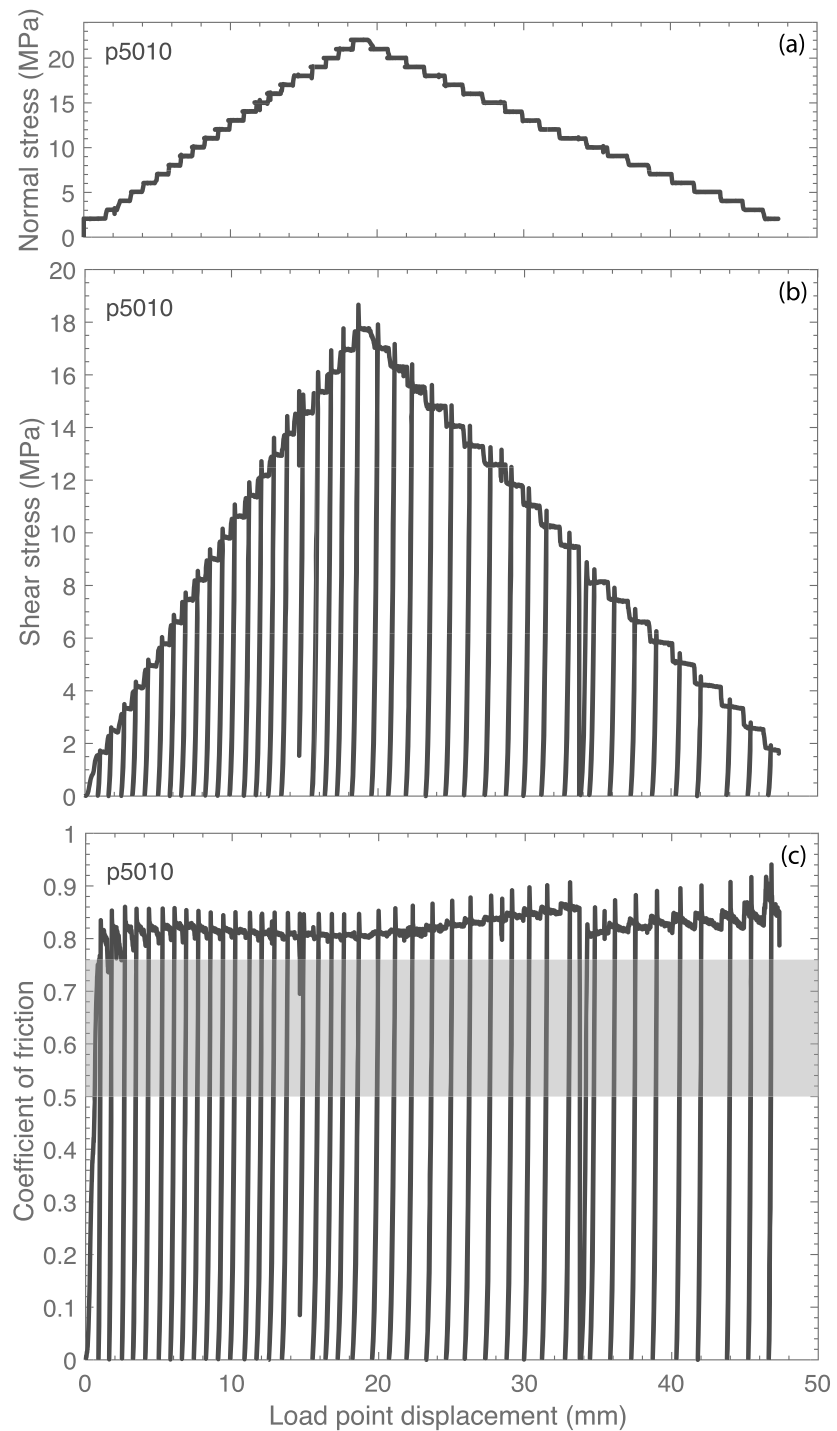
Figure 4. Results of an experiment with unload-reload cycles to measure shear loading stiffness. (a) Imposed normal stress history. (b) Shear stress response. (c) Coefficient of friction. Stiffness is measured from the linear portion of the friction-displacement curve during reload, denoted by the grey region.

We combine our friction data with continuous measurements of elastic wave properties derived from *P* wave amplitude (Figure 2) in two forms. First, absolute values of the ultrasonic amplitude (red segment of the waveform in Figure 2 inset) are presented as the squared root of the raw amplitudes measured in bits. The square root form (Nagata et al., 2012) accounts for the fact that the ultrasonic pulses propagate
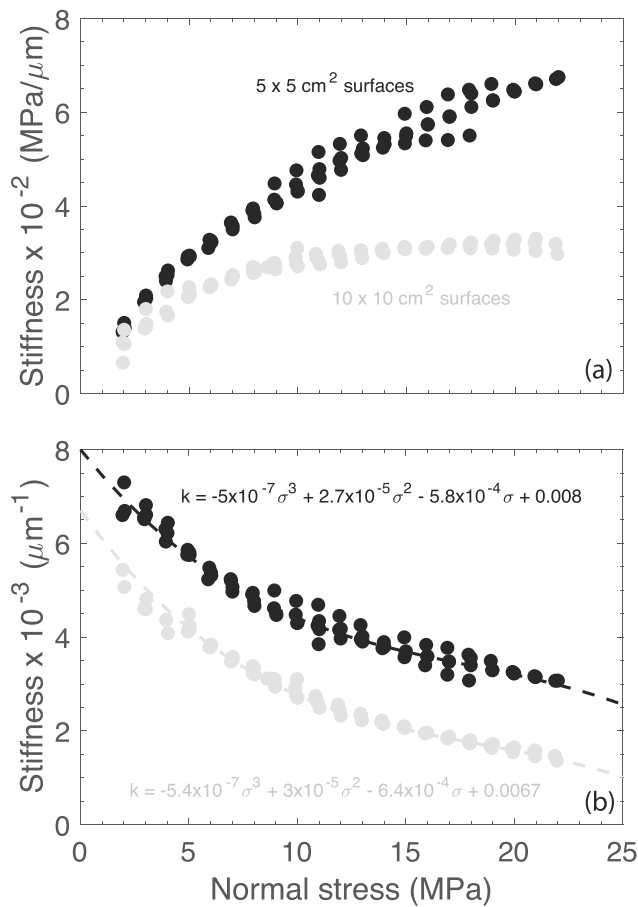
Figure 5. (a) Loading stiffness as a function of normal stress (see Figure 4) showing (b) inverse trend with increasing normal stresses when stiffness is normalized by the normal stress. The black and grey points represent measurements for granite samples with nominal contact area of 25 and 100 cm^2, respectively. The dashed lines in (b) show third-order polynomial fits. Note that apparent scatter in stiffness for a given normal stress is due to the second order effect of shear displacement; stiffness changes by this amount for 40-50 mm of shear offset (see Figure 4c).

through two fault surfaces (Appendix A). The second form normalizes the amplitude by a reference amplitude when it becomes important to eliminate bulk propagation effects through the granite blocks.

3. Results

Our type 1 sets of NSS for shear loading velocities of 11, 21, 42, and 64 µm/s (Figure 3). Previous works document the effect of net shear displacement on friction (Richardson & Marone, 1999; Tullis & Weeks, 1986). We did not explore the role of shear displacement directly, but we ran trial experiments with the reverse shear velocity history (faster to slower) and found that the effect of velocity history was minimal. For the results presented here we ran the same shear velocity history and compare results for the same net shear displacement range. We did not study step decreases in normal stress because they resulted in unstable sliding, which makes it difficult to interpret the response (Hong & Marone, 2005).

We also ran experiments to measure loading stiffness for our range of conditions (Figure 4). These tests involved shear load/unload sequences for a range of normal stresses. Shear loading stiffness was measured from the linear portion of the friction-displacement curve, as shown by the grey region of Figure 4c (between friction values of 0.5-0.7). For ease of comparison, we express stiffness in units of MPa/µm and normalize stiffness values by normal stress and report stiffness in units of 1/µm (Figure 5). The normalized shear stiffness decreases systematically with increasing normal stress, consistent with previous results (Leeman et al., 2015, 2016; Scuderi et al., 2017). Note that the stiffness is higher for the smaller samples, because we are measuring the composite stiffness of the testing machine and DDS configuration. The machine stiffness is known independently from calibration, and the values we obtain (Figure 5a), in the range of a few MPa/µm of shear displacement for normal stress of 1 MPa, are consistent with expectations for our sample size and the elastic properties of westerly granite. To interpolate the stiffness between each 0.5 MPa interval in normal stress, we fit the data with a third-order polynomial (Figure 5b).

3.1. Response to NSSs

In response to a NSS at constant shear loading rate, we observe a three-stage response, which is illustrated for a large NSS, from 8.5 to 13 MPa in Figure 6. The first stage is an abrupt increase in shear stress due to elastic coupling and Poisson expansion of the sample in the vertical direction (Figure 2). The measured increase in shear stress, generally <10% of the total increase in shear strength, is consistent with a Poisson ratio of 0.25 for westerly granite (Richardson & Marone, 1999). Both shear stress and elastic wave speed exhibit an immediate increase upon the NSS, noted as $\tau_{poisson}$ and A_σ in Figure 6b. Shear stress then increases linearly with shear loadpoint displacement until the point marked τ_α, consistent with the results of Linker and Dieterich (1992). Following Richardson and Marone (1999) and Hong and Marone (2005), we calculate a moving-window slope of the shear stress versus load point displacement curve immediately following the increase in normal stress. We define τ_α as the end-point of the window where the least squares best fit slope deviates by more than 5%. The P wave amplitude also increases during this interval and reaches a maximum, noted as A_α, that coincides with the end of the linear elastic increase in shear stress (Figure 6b). The third stage of the NSS response involves a nonlinear increase in shear stress and a decrease in wave amplitude each of which reach a steady state value (noted τ_{ss} and A_{ss}) at the same shear displacement, which is roughly 100 µm in Figure 6. See also Figure S1 in the supporting information, which shows the three-stage response for different NSS sizes. The grey region in Figure 6b shows the stiffness evolution constrained from our calibration experiments (Figure 5). Note that stiffness increases with increasing
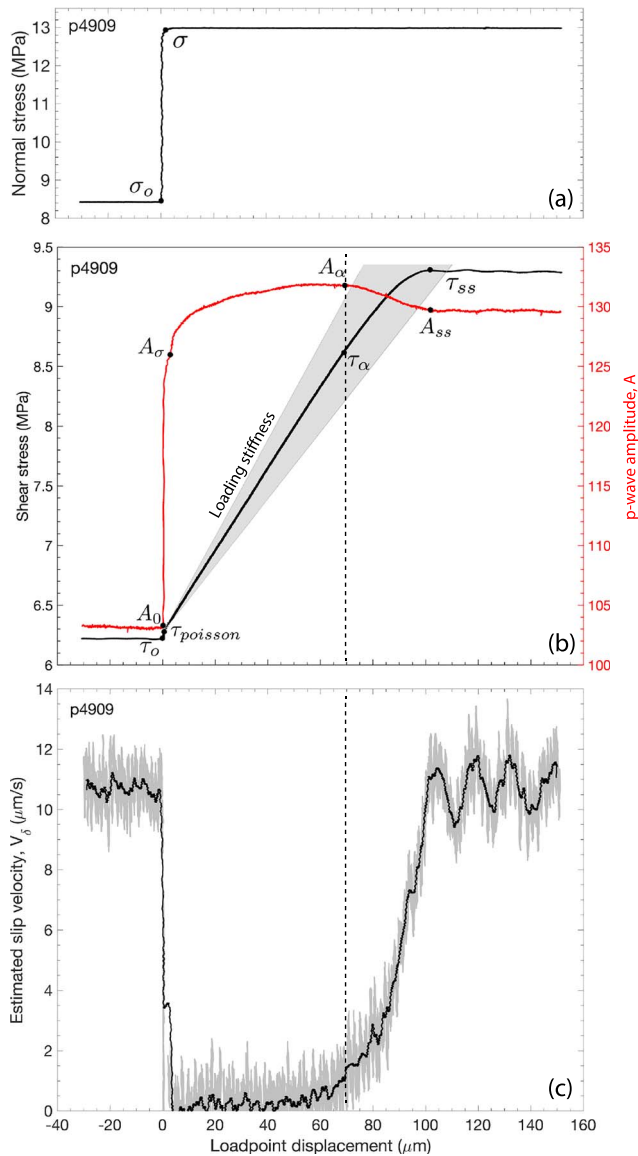
Figure 6. Data for a normal stress step experiment showing (a) normal stress history (b) shear stress (black) and ultrasonic amplitude (red), and (c) fault slip velocity (grey) and a smoothed moving average (black). τ_α marks the end of the linear, elastic, portion of shear stress increase, and A_α is the P wave amplitude at that point. τ_{ss} and A_{ss} and are the values for steady state sliding at the new normal stress. $A\sigma$ is the P wave amplitude at the time normal stress has reached its new value. The grey region in (b) shows the stiffness evolution as constrained from calibration (Figure 5). Note that stiffness increases with increasing normal stress from the lower to the upper limit of the grey region (see Figure 5a). Fault slip velocity is determined from the loadpoint displacement and stiffness (adjusted for normal stress) determined from the slope of the shear stress evolution in (b).

normal stress (Figure 5b), and thus, the expected elastic response transitions from the slope defined by the lower to the upper limit of the grey region (Figure 6b).

Our experimental boundary condition is constant load point velocity. We determine fault slip velocity using the measured elastic loading stiffness (Figure 6b). For our configuration, the fault slip rate V_δ can be expressed as a linear function of the time-rate of change of friction μ for loading stiffness k and load point velocity V_{lp} as:

$$\frac{d\mu}{dt} = k\left(V_{lp} - V_\delta\right) \tag{1}$$

We find that the estimated fault slip velocity drops immediately upon the NSS and remains at a low value, near zero, during the stage of elastic shear loading (Figure 6c). The slip velocity begins to increase at the point marked τ_α and reaches the initial, pre NSS, value at the same point at which shear stress and P wave amplitude reach steady state values.

The three-stage response we observe is consistent with observations by Linker and Dieterich (1992) and others (Boettcher & Marone, 2004; Hong & Marone, 2005; Richardson & Marone, 1999), who reported an instantaneous increase in shear stress and a longer-term transient evolution to a steady state shear strength over some characteristic slip distance or time. This is in contrast to the results of Kilgore et al. (2012, 2017), who report a single-stage behavior in which shear stress evolves nonlinearly with slip (or time) to a new steady state value. Indeed, the linear slope of our shear stress evolution curve is lower than the stiffness at the higher normal stress. This indicates that the fault is not fully locked but slipping slowly and/or that stiffness evolves with slip. If the faults were fully locked and the stiffness increase was instantaneous, the slope of the shear stress increase (Figure 6b) would coincide with the stiffness at the higher normal stress.

We can also evaluate the variations in shear strength and acoustic properties as a function of the estimated fault slip (Figure 7). The evolution of shear stress prior to reaching τ_α, at approximately zero slip, is correlated well with the overshoot in ultrasonic amplitude from A_σ to A_α (Figure 7b). Subsequently, the amplitude falls off to a steady state value as shear stress rolls off nonlinearly to the new steady shear strength (see inset to Figure 7b). The estimated fault slip velocity goes to zero instantaneously upon the NSS and subsequently increases, at a nearly constant acceleration, to the imposed background load point velocity. During the time period between the increases in normal stress to the onset of accelerated creep (τ_α), the fault apparently slips up to 1 μm (Inset to Figure 7b). At an imposed load point velocity of 11 μm/s, the fault slips up to 1 μm over ~7 s, which results in an average slip velocity of ~0.15 μm/s. This represents a nominal slip rate reduction of approximately 2 orders of magnitude across the NSS.

3.2. Slip and Time-Dependent Changes in Friction Upon a Change in Normal Stress

In response to a NSS, we find a linear-elastic increase in shear stress followed by an inelastic response. We measure the Linker and Dieterich (1992) α parameter from $\Delta\tau_\alpha$, (Figure 1), which is related to the size of the NSS as:
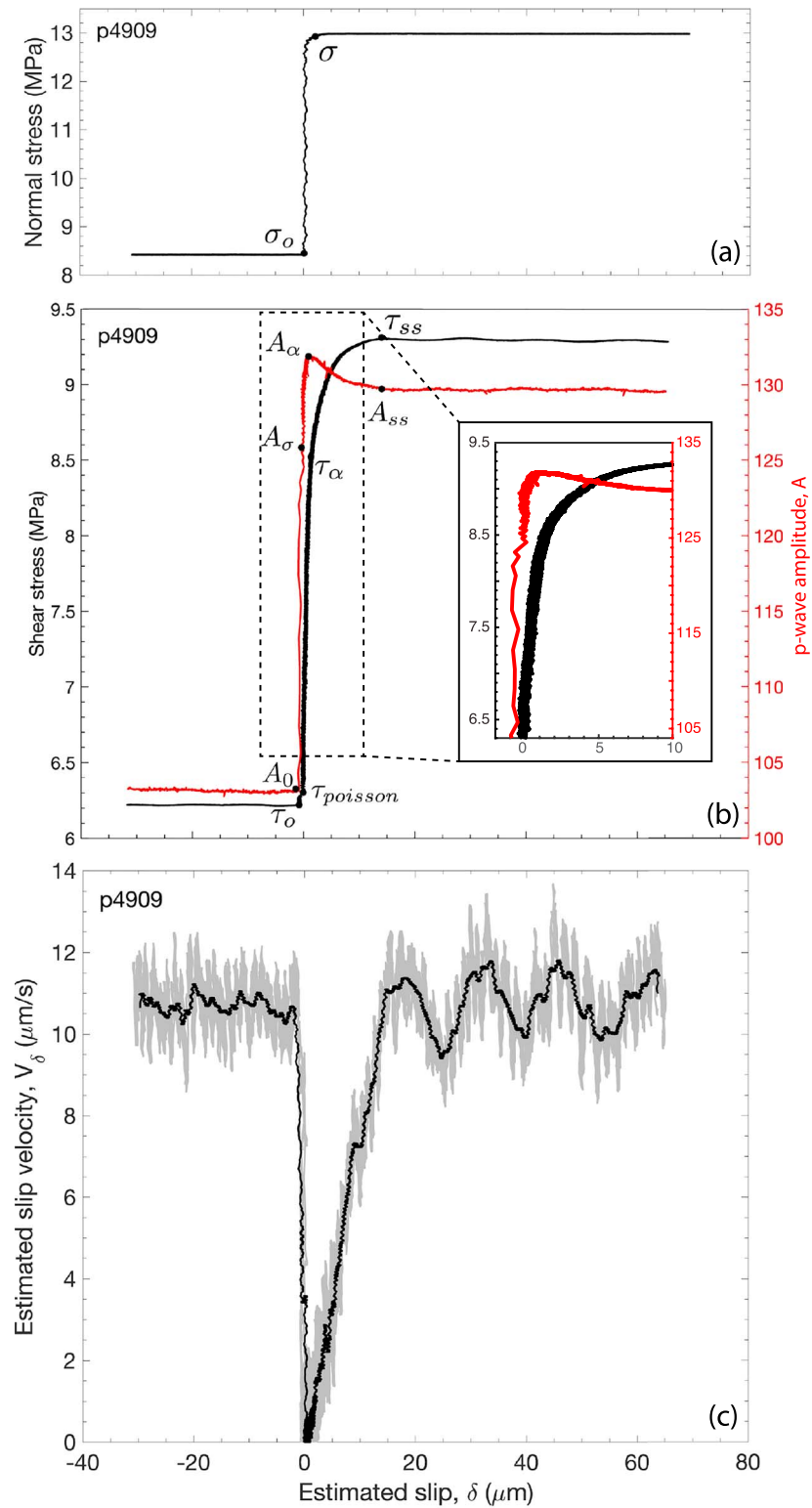
Figure 7. Data from Fig. 6 plotted versus estimated fault slip showing (a) normal stress, (b) shear stress and *P* wave amplitude, and (c) fault slip velocity. Annotation parameters are defined in Figure 6. Note the initial overshoot of *P* wave amplitude at zero slip, followed by decay to the steady state value as slip velocity increases back to its initial value.
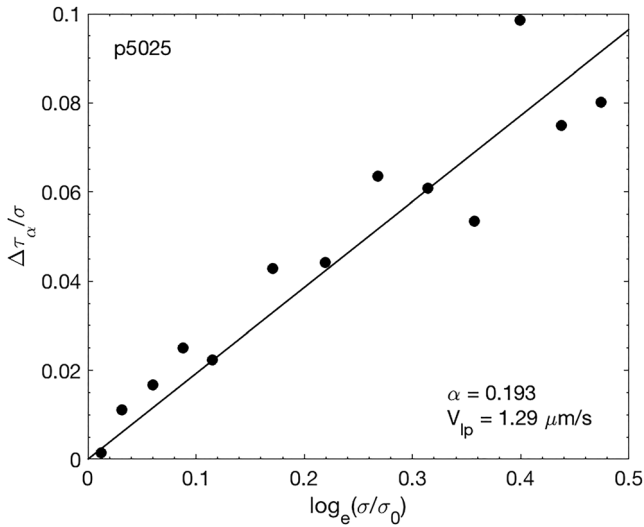
Figure 8. Relation between nonlinear strength increase $\Delta\tau_\alpha$ and the magnitude of the normal stress change. These data define the Linker and Dieterich (1992) parameter "α," which is the slope through the origin. The solid line shows least squares best fit to our data.

$$\alpha = \frac{\left(\frac{\Delta\tau_\alpha}{\sigma}\right)}{\ln\left(\frac{\sigma}{\sigma_o}\right)} \quad (2)$$

Microphysically, the immediate change in shear stress upon a NSS is consistent with Coulomb friction and can be interpreted as the result of the instantaneous increase in real contact area. Along the same lines, the additional increase in frictional strength associated with α could represent a shear (or time)-dependent increase in contact area and/or an increase in contact strength (so-called quality) at fixed area. This suggests that the average contact age decreases immediately upon a positive NSS, thus reducing the average value of frictional state. We explore these ideas by measuring the associated changes in elastic wave properties.

We find that the slip-dependent component of the change in friction for a NSS varies linearly with the logarithm of the NSS, consistent with equation (2) (Figure 8). The data in Figure 8 include all normal stress upstep sequences for 100% RH and load point velocity of 1.29 μm/s (Table 1). A linear best fit to these data with a zero-intercept yields a value of α=0.19 (Figure 8). We also measured α for a range of shear velocities and RH, and these data are included along with values from the literature in Figure 9, which has a y axis range that corresponds to the theoretical range of α, which can vary from 0 to the coefficient of friction.

Our measurements of α are similar to those reported in other studies and do not suggest a systematic variation with slip velocity or humidity (Figure 9). The values for granular fault gouge are higher than those for bare surfaces, but the difference is not large (Figure 9). Hong and Marone (2005) also measured α for a range of conditions, albeit over a smaller subset of the parameter space explored in this study. They interpret the lack of variation of α with velocity or humidity as a property of the bare granite surfaces, which do not produce significant gouge or wear products on the fault surfaces over the course of the experiment. They interpreted variations in α with fault velocity and RH as a property of granular friction (Hong & Marone, 2005). In our experiments, we find that the α values fall between 0.1 and 0.2, averaging ~0.16 (Figure 8), which is consistent with the theoretical value of 0.21 for Hertzian contacts (Molinari & Perfettini, 2017).
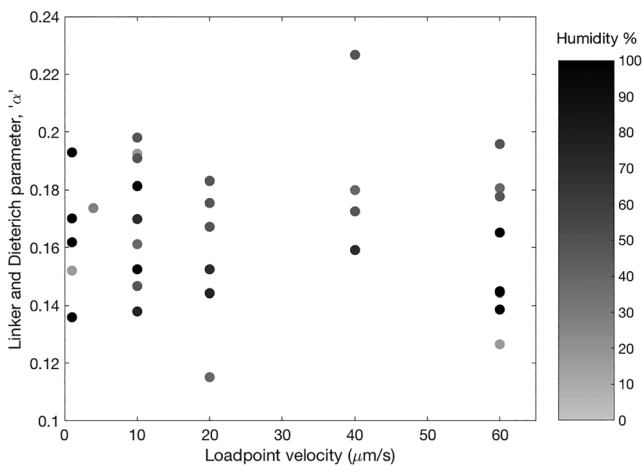

Figure 9. Summary of measurements of the parameter α plotted as a function of shear velocity and relative humidity during the tests. The unfilled symbols represent data sets with unknown humidity.

4. Discussion

4.1. Rate-State Friction Modeling of NSSs

The practical utility of calculating α experimentally is that it quantifies the perturbation in frictional state in response to a rapid, near instantaneous change in normal stress. This can then be used to solve the coupled rate-and-state partial differential equations and realistically model earthquake physics (e.g., Fang et al., 2011; He & Wong, 2014). However, given the apparent discrepancy in observations (Figure 1), the question remains as to whether traditional RSF evolution laws can be applied to satisfactorily model our observations. Here we discuss results for RSF forward models calculated for our experimental conditions to better probe the microphysical origin of the observed shear stress response.

In the RSF framework, shear stress, τ, is expressed as a function of the coefficient of friction, μ, and the normal stress on the fault, σ, as

$$\tau = \mu\sigma \quad (3)$$

where friction varies with slip rate and fault state as

$$\mu = \mu_0 + a \ln\left(\frac{V}{V_0}\right) + b \ln\left(\frac{\theta}{\theta_0}\right) \tag{4}$$

In equation (4), μ_0 is the coefficient of friction at a reference state θ_0 for steady sliding at velocity V_0. The parameters V and θ are the fault slip velocity and frictional state, respectively. Parameters a and b are material constants that may have second-order dependencies on velocity, humidity, temperature, normal stress, shear strain, etc. (Dieterich & Conrad, 1984; Mair & Marone, 1999; Marone, 1998a; Niemeijer & Spiers, 2006; Saffer & Marone, 2003).

Frictional state is usually interpreted as some measure of the microphysical contact quantity (real area of contact) or quality (contact shear strength). However, given that this cannot be measured directly, many empirical formulations for the evolution of state in the presence of perturbations have been introduced in literature (e.g., Marone, 1998a). Of these, the two commonly used ones are the Aging law (or Dieterich law; Dieterich, 1979) and the Slip law (or Ruina law; Ruina, 1983). These laws can be mathematically formalized as

$$\frac{d\theta}{dt} = 1 - \frac{V\theta}{D_c} \quad \text{(Aging law)} \tag{5}$$

$$\frac{d\theta}{dt} = -\frac{V\theta}{D_c} \ln\left(\frac{V\theta}{D_c}\right) \text{(Slip law)} \tag{6}$$

The parameter D_c is a critical slip distance over which the microscale contacts are renewed (Dieterich, 1979; Marone & Kilgore, 1993; Ruina, 1983; Scholz, 2002). At steady state, $\theta = D_c/V$ and hence, state, with units of time, is also interpreted as a measure of contact lifetime, as suggested by Rabinowicz (1951, 1956). The fundamental difference between the Aging and Slip laws is that while the Aging law allows state to evolve with both time and slip, the Slip law only allows state evolution with slip (Bayart et al., 2006; Bhattacharya et al., 2015, 2017).

In addition to the definition of α from equation (2), the parameter α can also be defined as a function of state (equation (10) of Linker & Dieterich, 1992):

$$\Delta\tau_\alpha = b\sigma \ln\left(\frac{\theta}{\theta_0}\right) \tag{7}$$

Substituting equation (7) in equation (2) gives

$$\theta = \theta_0 \left(\frac{\sigma_0}{\sigma}\right)^{\alpha/b} \tag{8}$$

Differentiating equation (8) with respect to time allows us to modify equations (5) and (6) to:

$$\frac{d\theta}{dt} = 1 - \frac{V\theta}{D_c} - \frac{\alpha\theta}{b\sigma}\frac{d\sigma}{dt} \tag{9}$$

$$\frac{d\theta}{dt} = -\frac{V\theta}{D_c} \ln\left(\frac{V\theta}{D_c}\right) - \frac{\alpha\theta}{b\sigma}\frac{d\sigma}{dt} \tag{10}$$

We simultaneously solve equations (1), (4), and (8) with the state evolution relations (equations (9) or (10)) as a set of coupled partial differential equations to model the effect of NSS increases. Specifically, our forward model uses a fifth-order Runge-Kutta solution with adaptive step size (Press et al., 1992). Given that we implement the normal stress increase as an ideal "step" in the forward models, the perturbation of state due to the step change occurs at the start of the iterative solution based on equation (8); thus the, second differential term in equations (9) and (10) has no effect on the overall solution scheme; that is, the time derivative of normal stress is zero after the first iteration (Richardson & Marone, 1999). Note that equation (7) ignores the impact of slip rate excursions on friction and frictional state, which inevitably occur during a NSS (see Bhattacharya, 2017 for a novel treatment of this problem within the RSF framework.)

Here we discuss the evolution of frictional state by invoking a subtle variation relative to equation (4). We transform the logarithmic term for state in equation (4) by redefining state as φ where

$$\varphi = b\sigma \ln\left(\frac{\theta}{\theta_0}\right) \tag{11}$$

This definition recasts state as a measure of strength rather than simply describing it as a contact lifetime (Linker & Dieterich, 1992). Here it is convenient because it allows us to directly probe the relationship between state and ultrasonic amplitude if the amplitude is indeed a proxy for contact area as has been previously suggested (Nagata et al., 2014).

Figure 10 shows the forward model solutions for the Aging and Slip laws using our lab parameters. The lab data and model results are offset so that the NSS, from 8.4 MPa to 13 MPa, occurs at zero load point displacement and fault slip, that is, the zero crossing on the *x* axis in Figure 10. The Slip law model better fits the shear stress evolution data as compared with the Aging law (Figure 10), which overshoots shear stress at the initial stages of slip acceleration. Interestingly, Hong and Marone (2005) document that the Slip law model better fits their experimental data on clay/quartz gouge layers as well. The slight offset in initial shear stress between experimental and forward model can be attributed to the assumption of constant coefficient of friction at all normal stresses in the numerical models, whereas the experiments indicate a subtle, second-order effect of normal stress on the coefficient of friction (Figure 10). Similarly, the estimated on-fault slip velocity from the experimental shear stress curve is better fit by the Slip law model (Figures 10c and 10d). The Slip law model also captures the subtle overshoot in slip velocity observed in Figure 10c at a load point displacement of ~100 μm (or slip of ~18 μm in Figure 10d). Additionally, the Slip law model preserves the total amount of slip required to reach the new steady state shear strength, whereas this value is overestimated by the Aging law model. The decrease in frictional state in response to a sudden increase in normal stress is seen in Figures 10e and 10f. However, since ultrasonic amplitudes increase in response to a normal stress, we compare the ultrasonic amplitudes to the sum of the frictional state (equation (11)) and the steady state term $\mu_0\sigma$ (equations (3) and (4)). This ensures that the sense of direction across a step increase in normal stress is positive for both ultrasonic amplitude and frictional state (Figures 10g and 10h). Interestingly, the ultrasonic amplitude appears to qualitatively favor the Aging law model of state evolution rather than the Slip law (Figures 10g and 10h)). Because the slip velocity approaches zero (~10^{-6}–10^{-8} μm/s from forward models), the Slip law state appears to increase infinitesimally or not at all whereas the Aging law state, as defined by equation (11) increases nearly logarithmically with time.

One way to explain these contrasting observations is by arguing that for conditions far from steady state ($\theta \ll D_c/V_{lp}$) state and contact area are not interchangeable in NSS experiments. In other words, we can consider the ultrasonic amplitude (Nagata et al., 2014) and the Aging definition of state (Beeler et al., 1994; Dieterich & Kilgore, 1994) as being proxies for time-dependent contact area increase only. Simultaneously, if the Slip law definition of state depends on some combination of contact area and contact shear strength that requires finite fault slip, then state should not evolve until the locked fault starts slipping. The importance of contact quality (or strength) in addition to contact area in the context of state evolution has been demonstrated in classical velocity step and slide-hold-slide experiments (Bhattacharya et al., 2017; Nagata et al., 2008, 2012, 2014; Thom et al., 2017; Tian et al., 2017); thus, invoking its importance in the presence of NSSs and low slip rates is not unreasonable. One can imagine a case where a NSS increase results in newly created contacts that have a finite shear resistance, which is lower than the shear resistance of the older preexisting contacts (e.g., Bhattacharya, 2017). In this case, a reduction in state across a NSS increase can be interpreted as a reduction in some combination of contact area as well as contact strength. A similar line of reasoning was invoked by Hong and Marone (2005), and they suggest that the "younger" (and smaller) contacts created in response to a NSS would be the weakest, and hence first to be destroyed during a step decrease in normal stress. This view assumes that the contact strength evolves with slip and allows the possibility that different contacts have different strengths.

The idea of scale-dependent strength at contact junctions has been observed in both the field (Brodsky et al., 2016) and experimentally via nanoindentation tests (Thom et al., 2017). Moreover, Bureau et al. (2002) and Li et al. (2011) have reported independent experimental observations suggesting that contact quality (or contact shear strength) can evolve with slip (or time) even if contact area is kept constant, as suggested by Li and
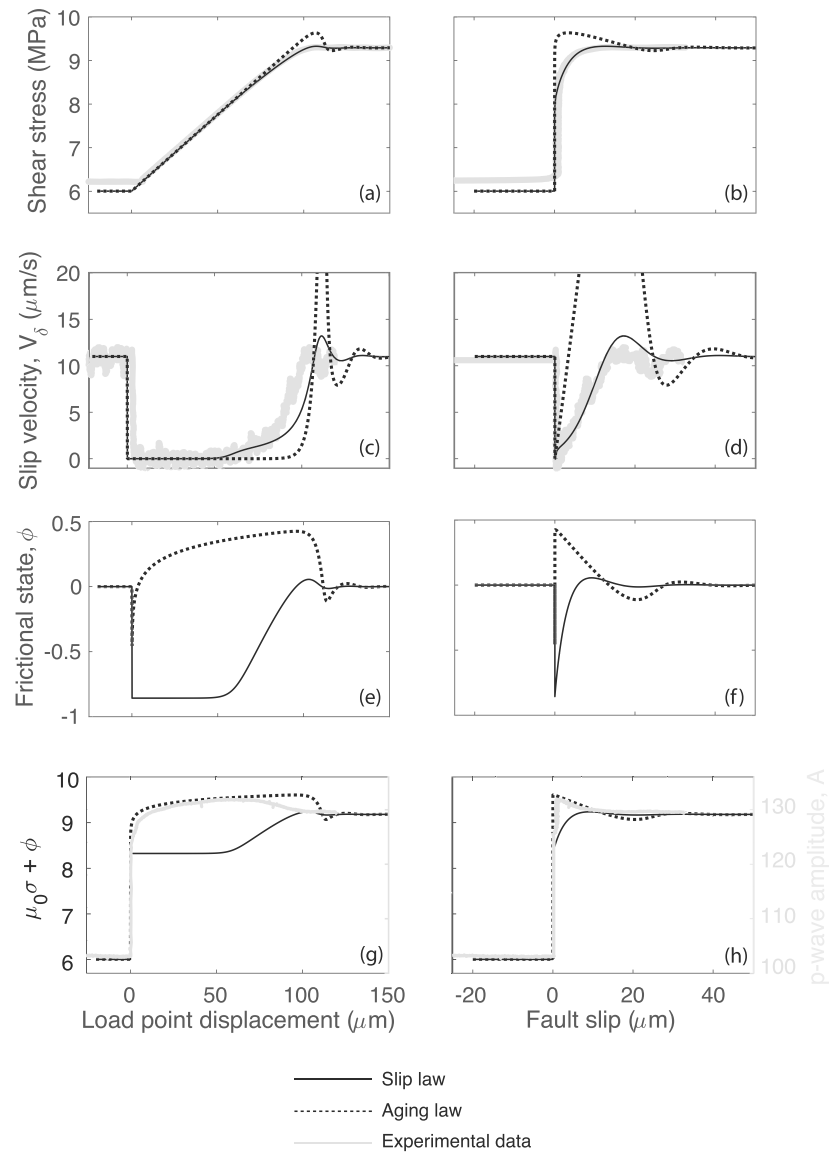
Figure 10. Forward models and experimental data showing (a and b) shear stress, slip velocity (c and d) shear stress, (e and f) frictional state, and the (g and h) sum of frictional state and reference friction along with P wave amplitude. Overall, the Slip law fits the evolution of shear stress and slip velocity better than the Aging law, although neither law does particularly well with the increase in velocity after it drops. Note that the form of the increase in wave amplitude is more similar to the Aging law state evolution than the Slip law. RSF models use $a = 0.0091$, $b = 0.0106$, $D_c = 3.5$ μm, $k = 0.0027/$ μm, and $\alpha = 0.17$, as determined from velocity step tests carried out in experiments at comparable shear displacements. Data from experiment p4909.

Rubin (2017). Specifically, because contact junctions are essentially dislocations that slide in and out of existence, any process that fundamentally changes or affects the junction boundary will change the contact shear strength with slip. That is, when a single asperity slides, it starts to slip along the boundaries parallel to the direction of shear, which are like mode III cracks (Sharp et al., 2017). This provides an opportunity for adsorbed impurities on the interfaces to diffuse in or out of the contact junction and change contact quality and, in turn, state. In other words, physico-chemical processes at the junction perimeter may influence contact strength (Bureau et al., 2002; Ikari et al., 2016; Li & Rubin, 2017; Renard et al., 2012). In summary, we suggest that transient slip and the associated contact-scale plastic deformation is a necessary prerequisite for state evolution, where state evolution is described as a combination of real contact area (quantity) and contact strength (quality).
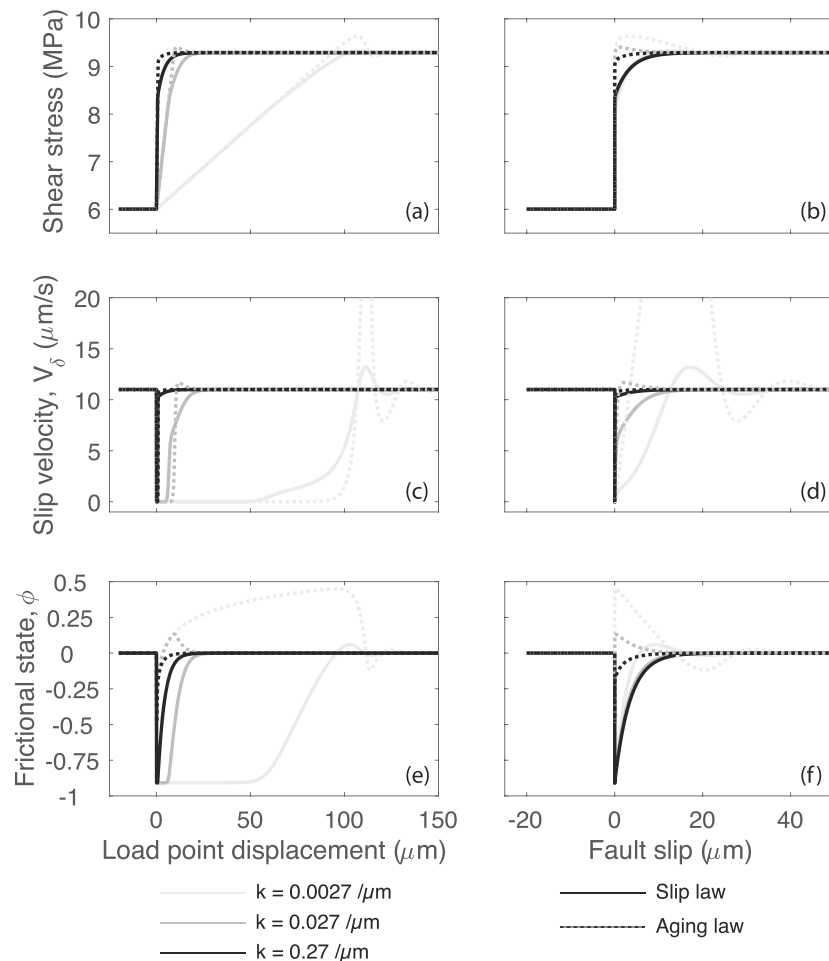
Figure 11. Numerical simulations of data shown in Figure 10 illustrating the effect of different loading stiffnesses on (a and b) shear stress, (c and d) slip velocity, and (e and f) frictional state. The duration of the slip rate excursion following a normal stress step scales inversely with stiffness, which has a big effect on state evolution and the peak value of state. The lowest value of stiffness corresponds with our lab values (Figure 5 and 10). RSF simulations used $a = 0.0091$, $b = 0.0106$, $D_c = 3.5$ μm, and $\alpha = 0.17$.

Based on the results from our NSS and unload-reload experiments (Figures 5–7), we suggest that the discrepancies between different observations of shear stress evolution for NSS (Figure 1) can be reconciled by accounting for the strong dependence of fault slip rate on loading stiffness. Stiffer configurations result in a smaller slip rate excursion across a NSS, which would in turn imply a faster (in time) march to steady state velocity.

We explored the effect of stiffness on fault slip velocity during a NSS by performing a set of numerical simulations with different stiffnesses (Figure 11). The lowest stiffness used in our simulations (0.0027 μm⁻¹) corresponds to our experimental stiffness, and the highest stiffness is 100 times larger. The loading stiffness reported in the Kilgore et al. (2012, 2017) experiments is approximately 0.15 μm⁻¹ at a normal stress of 5 MPa and hence is approximately represented by the high stiffness in our simulations (Figure 11).

Shear stress evolution in our Aging law simulations has a steeper slope and consistently overshoots the peak shear strength compared to our lab data (Figures 11a and 11b). The total slip required to reach the new steady state shear strength is independent of stiffness in the Slip law simulations, whereas the lowest stiffness simulation appears to require the largest amount of slip in the Aging law simulations. Microphysically, the conservation of slip is appealing for sliding interfaces because the loading stiffness should have no effect on the number/size of new contacts created due to an increase in normal stress. The
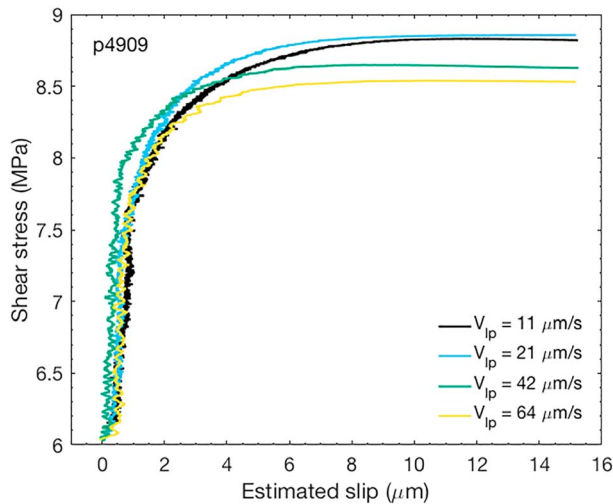
Figure 12. Data showing shear stress as a function of fault slip for a 3.7 MPa (45%) normal stress step at four different loading velocities. See Figure 3 for experiment run history. Note that the characteristic length scale required for the shear stress to reach a new steady state does not vary systematically with loadpoint velocity.

models of slip rate (Figures 11c and 11d) indicate that stiffer faults have shorter slip rate excursions, after which they accelerate rapidly to the imposed load point velocity. The Aging law simulations also predict consistently higher accelerations as well as overshooting velocities, the magnitude of the latter being inversely related to the system stiffness. Longer duration slip rate excursions for the Aging law allow state to evolve to a larger magnitude at lower stiffnesses, whereas this overshoot in state is barely discernible at higher stiffness, which is similar to the contrasting observations in ultrasonic amplitudes between Kilgore et al. (2017) and our study (Figures 11e and 11f). On the other hand, the Slip law state does not evolve when the fault is effectively locked and only evolves with accumulating slip. Slip begins nearly immediately in the high stiffness case as compared to the lowest stiffness model. In other words, the Slip law and Aging law simulations are asymptotically similar at higher stiffnesses; that is, the difference between the description of state as being purely contact area versus a combination of quality and quantity becomes less important. This is because the fault locks up for a very small amount of time, allowing negligible opportunity for time-dependent healing, and the onset of accelerated slip is nearly instantaneous, as is the evolution of state. Parameterizations of the NSS size and values of the Linker and Dieterich α parameter for different stiffnesses are reported in Figures S2 and S3 of the supporting information.

4.2. Slip as a Control on Shear Stress Evolution

We further test the robustness of our observations via a detailed analysis of fault slip. We observe the evolution of shear stress for the same NSS, conducted at different imposed load point velocities, keeping other boundary conditions constant (Figure 12). An immediate observation is that the shear stress reaches steady state over a constant slip distance of ~6 μm independent of imposed loading velocities. This indicates that at least to a first order, the friction micromechanics are dominated by slip (rather than time); a finite slip is required to renew contacts and establish a new steady state following a NSS.

We also address whether the size of the NSS is more important in an absolute or relative sense. If contact area evolution in the NSS depends more on the step size in a relative sense, one might expect the amount of slip to be constant irrespective of whether the upstep goes from 2 to 3 MPa or 4 to 6 MPa. However, if the size of the upstep is more important in an absolute sense, an upstep from 2 to 3 MPa would require the same amount of slip as an upstep from 4 to 5 MPa. Figure 13 shows plots of slip versus the relative NSS size (Figure 13a) and slip versus the absolute increase in normal stress (Figure 13b). In both cases, the amount of slip required to reach steady state increases with the size of the normal stress upstep. A larger amount of slip is required to reach steady state for a larger increase in normal stress. Additionally, the figures clearly show that the NSS in an absolute sense regulates the amount of slip required to reach steady state since Figure 13b indicates that the amount of slip required to attain steady state sliding is proportional to the differential normal stress on the fault. Recasting this observation in the context of changes in real contact area, a clear implication is that a finite increase in normal stress proportionally increases the real contact area of the system. The amount of real contact area created, to a first order, depends not on the initial normal stress, but the absolute size of the increase in normal stress. As an example, a 50% increase in normal stress from 2 to 3 MPa and 10 to 15 MPa should both result in a 50% increase in real contact area. However, because the initial real contact area is smaller in the former case, the absolute increase in contact area is also smaller. As a consequence, the fault is required to slip a smaller distance to renew/increase its contacts to the new, larger contact area.

4.3. A Case for Ultrasonic Amplitude as a Proxy for Contact Area

Our results indicate a complex shear stress and fault slip velocity response to normal stress upsteps. The simultaneous and independent measurement of ultrasonic amplitudes helps elucidate some potential underlying microphysical processes. Specifically, we address whether the changes in wave amplitude truly reflect the changes in shear stress and/or slip velocity. We plot the amplitude response for the normal stress upstep from Figure 7 as a function of the corresponding shear stress and slip velocity in Figure 14. In Figure 14a, the
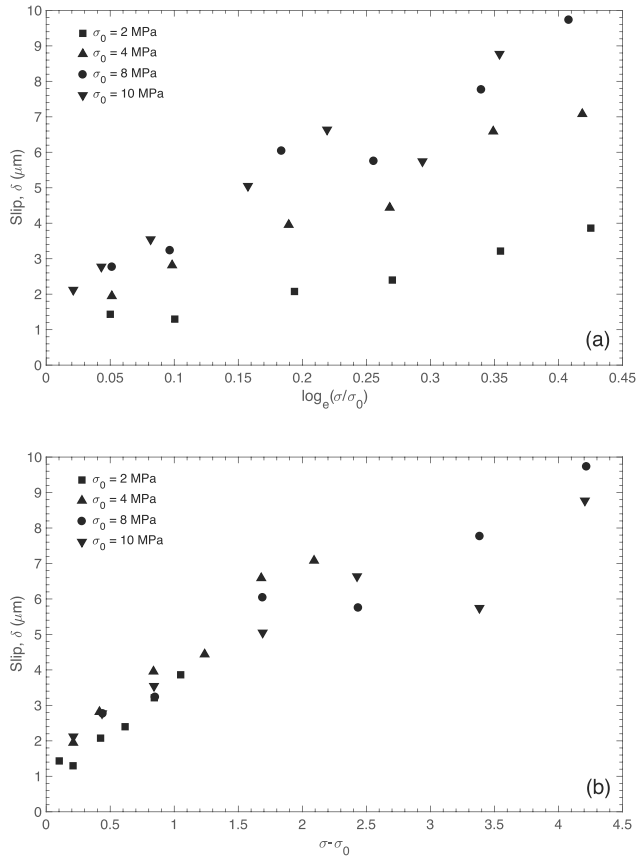
Figure 13. Fault slip required to reach steady state shear strength (see Figure 7 for slip velocity history) as a function of normal stress for four normal stress step sequences from σ_0 to σ. (a) Lognormalized normal stress. Slip does not collapse onto the same curve for different baseline normal stresses (b) slip versus the change in normal stress. Here the data collapse onto a single curve indicating that the size of the normal stress step is what determines the magnitude of the perturbation in friction.

initial amplitude corresponds to A_σ, that is, the lowest amplitude at the new, higher normal stress, before shear stress begins to increase. The transition from linear elastic to nonlinear shear stress evolution is marked as τ_α (dashed line). Note that wave amplitude increases at a decreasing rate as the shear stress linearly increases with load point displacement, reaching a peak value as the shear stress reaches τ_α. Thereafter, wave amplitude decreases, at a faster rate than it increased, for the remaining portion of the shear stress evolution. We observe a similar trend for the relationship between amplitude and slip velocity (Figure 14b). Initially, when the fault locks up in response to the NSS, wave amplitude increases to a peak, A_α. Subsequently, as the fault starts creeping, the amplitude slowly decreases to its steady state value, A_{ss}.

The relationship between P wave amplitude and fault slip suggests the possibility that amplitude could be a reliable proxy for the real contact area at the fault interface. This is based on two lines of evidence. First, an increase in real contact area in response to a rapid increase in normal stress and time-dependent contact-area increase at a constant normal stress with zero slip, that is, frictional healing during a hold, have both been documented previously in literature via optical observations of the real contact area (Dieterich & Kilgore, 1994; Nagata et al., 2014). Second, an inverse relationship between fault slip velocity and frictional state (when interpreted as an indicator of real contact area) is the basis of rate and state friction. Both sets of observations have been made for the ultrasonic amplitude in this study (Figure 14b).

We quantify the changes in ultrasonic amplitude as a function of changes in normal stress over a larger range of normal stresses than documented previously. Figure 15 shows the amplitude, A_{ss}, as a function of normal stress for four different NSS sequences performed at different load point velocities. A_{ss} increases linearly with normal stress over the range of normal stresses explored in this study. Interestingly, we also observe second-order changes in the amplitude across the different sliding velocities for a given normal stress. Specifically, the amplitude decreases logarithmically (inset to Figure 15) with increasing sliding velocity, which is similar to the rate-dependent contact area evolution predicted by rate and state friction.

We perform a least squares log linear fit to this curve and use the slope of this fit (-3.545) as a sensitivity parameter, r, to calibrate between ultrasonic amplitude, A, and frictional state, φ. Specifically,

$$r = \frac{\Delta A}{\Delta \varphi} = \frac{3.545}{b\sigma} \tag{12}$$

We refer the reader to Nagata et al. (2012) for a detailed treatment and derivation of equation (12). Using equations (11) and (12), we rewrite equation (8) as

$$\zeta = \frac{b\Delta A}{3.545} = \alpha \ln\left(\frac{\sigma}{\sigma_0}\right) \tag{13}$$

Note that equation (13) involves two assumptions about our understanding of the interrelationship between state (during steady state sliding), contact area, and ultrasonic amplitude: (1) There is no significant underlying difference in the physics of frictional state between two steady state velocities and two steady state shear stresses, and (2) the calibration parameter, r, does not exhibit significant first order dependence on normal stress over the parameter space explored. Because we have measured all quantities except α, which we estimated (Figures 8 and 9), we can use equation (13) to constrain α independently using information from the ultrasonic amplitude and NSS size. A plot showing ζ as a function of the NSS is shown in Figure 16. The zero-intercept slope of this line, in a least squares sense must be α, according to
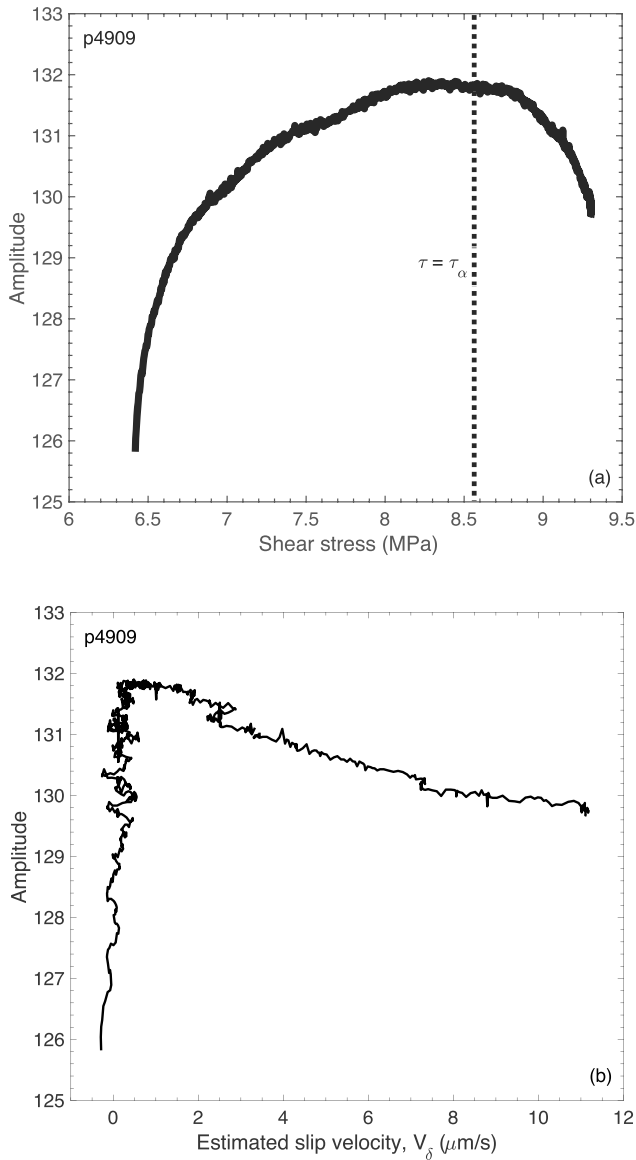
Figure 14. Data during a normal stress step from 8.5 to 13 MPa showing ultrasonic amplitude as a function of (a) shear stress and (b) fault slip velocity. The dashed line in (a) shows τ_α, defined by the end of the linear increase in shear stress associated with elastic loading (Figure 1), which corresponds to the peak value in panel (b) when slip velocity begins to increase. (a) Note that wave amplitude increases initially and then begins to plateau before the end of elastic loading. Shear stress continues to increase and wave amplitude decreases. (b) Note that wave amplitude increases when the fault is stationary ($V_\delta = 0$) and subsequently decreases to a steady state value as fault slip velocity increases to the background loading rate.

equation (13). We find that the slope of this line is ~0.17, which is in excellent agreement with our value of α estimated independently from the mechanical data, that is, $\Delta\tau_\alpha$ deduced from the shear stress versus load point displacement plot. This indicates that the ultrasonic amplitude is potentially a reliable proxy for frictional state and contact area at steady state.

To eliminate the effect of velocity and study the amplitude increase across the fault surface solely due to the normal stress upstep, we normalize and express the amplitude as the ratio A_σ/A_o and plot it versus the absolute difference in normal stress in Figure 17a and equivalent stress ratio σ/σ_o in Figure 17b. While the amplitude ratio increases with the size of the NSS, it forms two clusters corresponding to two baseline values of normal stresses used in the experiments (Figure 17a). To a first order, we observe no systematic variations between the amplitude ratios corresponding to different loading velocities. However, when plotted versus the normal stress ratios, the two curves collapse onto the same line. More importantly, the curves collapse close to the 1:1 line (dashed line) between the amplitude ratios and normal stress ratios. This allows us to write a constitutive law relating the time rate of change of amplitude and the rate of change of normal stress as

$$\frac{dA}{d\sigma} \approx \frac{A_0}{\sigma_0} \tag{14}$$

Equation (14) implies that the ultrasonic amplitude across the fault surface is proportional to the nominal normal stress, or normal force, on the fault. This is identical to the analytically determined relationship between the real area of contact and normal force for elastic contacts in a multicontact interface (Bowden and Tabor, 1951; Greenwood & Williamson, 1966).

However, any argument for describing amplitude as a proxy for contact area must also reconcile the analytical and experimental studies showing that amplitude is linearly related to contact stiffness (Kendall & Tabor, 1971; Kilgore et al., 2017; Pyrak-Nolte et al., 1990; Yoshioka & Iwasa, 2006). Additionally, contact stiffness for a single contact, k_0, of radius r is related to the elastic modulus, E, and a material constant, c, as

$$k_0 = cEr \tag{15}$$

In other words, the amplitude is linearly related to contact stiffness, which is, in turn, linearly related to the contact junction radius r rather than r^2 as would be necessary for describing real contact area. For a distribution of N asperities with average radius, r, the contact stiffness may be given as (Kendall & Tabor, 1971)

$$k = Nk_0 \tag{16}$$

Equation (16) applies to contacts where the real area of contact is less than 10% of the nominal (or apparent) area of contact, as is the case here (Dieterich & Kilgore, 1994; Yoshioka & Iwasa, 1996). We now combine our knowledge that the transmitted amplitude is linearly related to the total contact stiffness k and, in turn, to the number of contacts N, and the implication from Figure 17b that the amplitude increases linearly with normal stress as if it were representative of the real contact area ($N{\cdot}\pi r^2$). Together, these observations indicate that across a NSS, the real area of contact increases but the average contact dimension r does not.
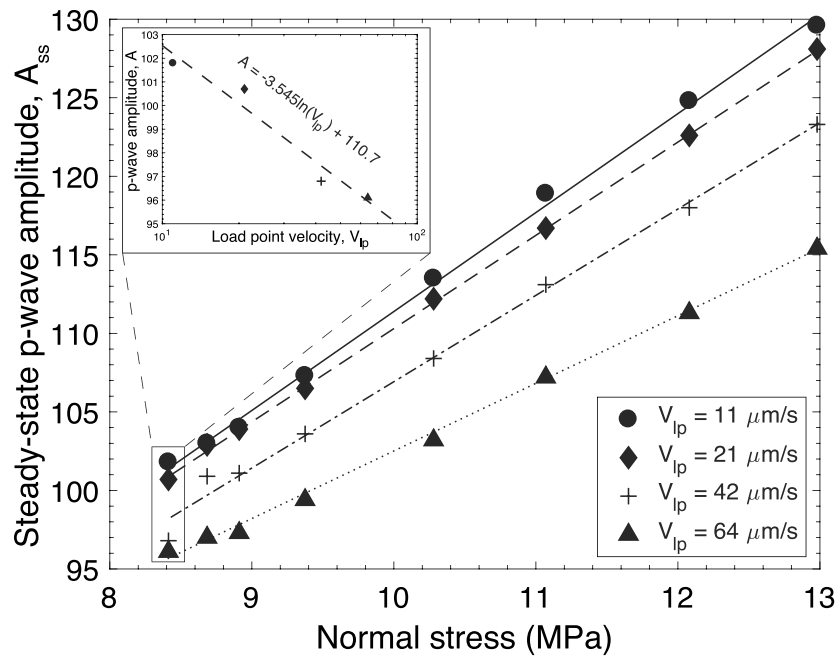
Figure 15. Measured steady state *P* wave amplitude as a function of normal stress for a series of experiments at different loading velocities. Note that *P* wave amplitude increases linearly with fault normal stresses, consistent with expectations for Coulomb failure and a linear increase in contact area with normal stress. For a given normal stress, wave amplitude decreases with increasing velocity, consistent with the idea that contact area is lower for higher slip velocity. Inset shows wave amplitude as a function of the log of loading velocity for 8.4 MPa. The slope of this log linear decrease (-3.54) is used to calibrate the sensitivity of the amplitude-state relationship. Fiducial lines represent least squares best fit lines to each data set.

Instead, a distribution of new asperities is created such that the total number of contacts *N* scales linearly with normal stress and the average contact dimension is conserved. This can also explain the linear scaling of slip with differential normal stress for small perturbations as documented in Figure 13b, because a linear increase in the number of contact junctions would imply a linear increase in the amount of slip they would have to undergo to reach a state of plastic deformation.
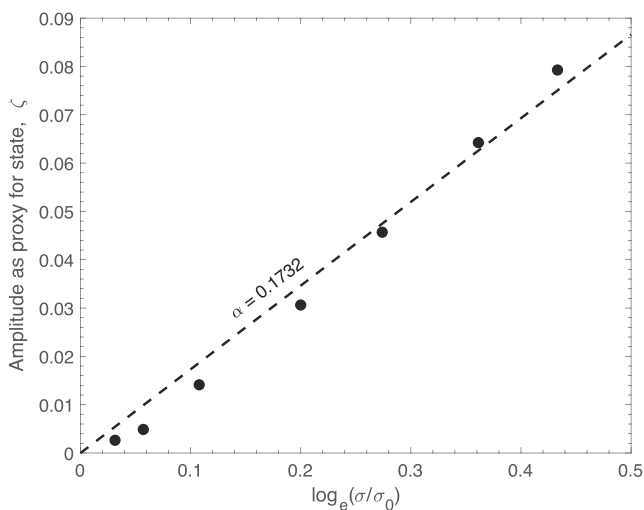
While we demonstrate that the relationship between *P* wave amplitude and contact area is approximately linear over the range of normal stresses explored in this study, the implications of these observations should be extrapolated cautiously to extremely small (or large) stresses. Moreover, our observations and that of other workers (e.g., Kilgore et al., 2017; Nagata et al., 2014) demonstrate the complexities involved with the study of *P* wave amplitude, in that it routinely exhibits long term drift during experiments perhaps due to the formation of wear product on the sliding interfaces. Nagata et al. (2014) also observe a nonunique relationship between *P* wave amplitude and contact area under various conditions. Other external factors such as temperature, humidity, and pore fluids could also affect the *P* wave amplitude in a complex manner as yet unquantified.

4.4. A Microphysical Model of Fault Slip for a NSS

Based on the observations of ultrasonic amplitude and slip, we devise a microphysical model of a distribution of Hertzian contacts that experience a rapid increase in normal stress while being sheared at a constant background sliding rate (Figure 18). Consider an initial distribution of contact

Figure 16. The Linker-Dieterich parameter "α" is constrained independently using ultrasonic amplitude as a proxy for state. Here the parameter "ζ" is the ultrasonic amplitude multiplied by a calibration parameter to account for state, expressed as a function of the normalized change in normal stress across an upstep. The slope represents the Linker-Dieterich parameter "α." Equations (12) and (13) provide the derivation.
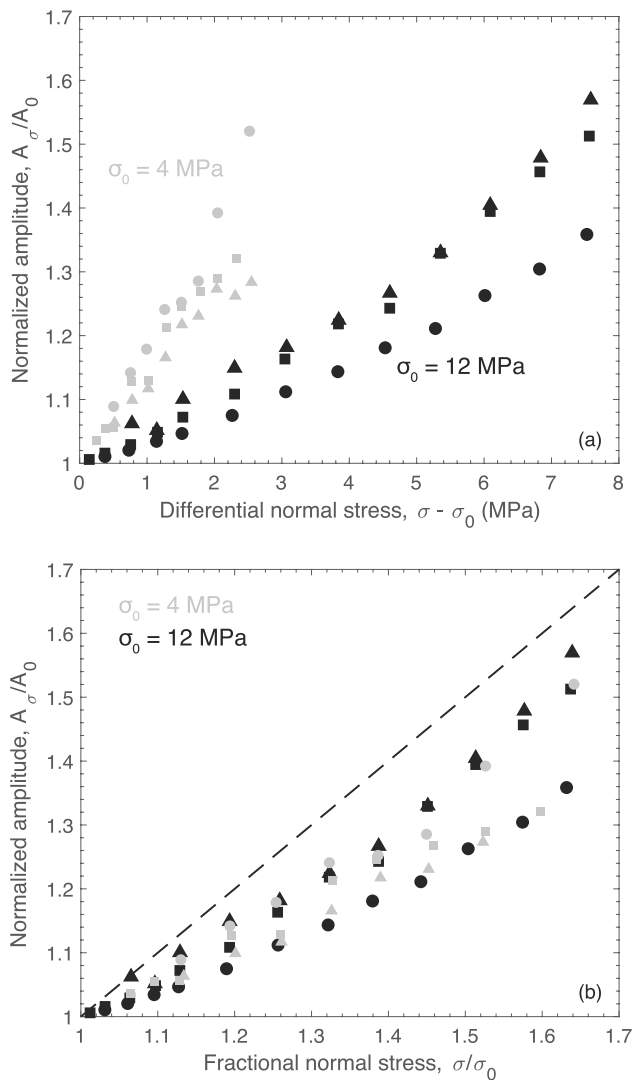
Figure 17. Normalized values of p-wave amplitude corresponding to normal stress steps as a function of (a) the differential change in normal stress and (b) the fractional change in normal stress for two different baseline values of normal stress. Note that the P wave amplitudes in (b) collapse on the same curve for the two baseline normal stress values, which suggests that the absolute value of the baseline normal stress is unimportant. Also note that the amplitude in (b) varies close to the 1:1 line (dashed line) with respect to the fractional increase in normal stress. The symbols—circle, square, and triangle, respectively, represent load point velocities of 1, 11, and 64 μm/s.

sizes with an average asperity radius r and a range of contact strengths. For a NSS, the real contact area increases elastically in accord with the magnitude of the stress step magnitude, independent of the sliding velocity (Figure 18b). New contacts are created, and existing contacts become bigger as has been observed optically for acrylic (Dieterich & Kilgore, 1994). Contact junctions also age and enlarge in proportion to the normal stress; and they are rejuvenated at a rate proportional to the rate of frictional sliding (e.g., Figure 6c). Further elasto-plastic growth of contacts is limited as the fault slip rate becomes appreciable. Subsequently, as the fault accelerates toward its imposed background loading rate, some portion of the fractional increase in contact area, perhaps involving the younger contacts with a lower shear resistance, is destroyed. Finally, when the fault is slipping at the imposed loading rate at its new steady state shear strength, all contacts are deforming fully plastically and this final contact area is due to a combination of the driving velocity and current normal stress. The net frictional strength is the product of contact junction size and quality (strength), as illustrated by the size and shading in Figure 18. A similar microphysical mechanism has been proposed for granular media by Richardson and Marone (1999) guided by their observation of layer thickness changes in response to a NSS. Note that the transmitted elastic wave amplitude follows this progression for a NSS, with an initial jump followed by a period of increase associated with low slip rate (Figure 6c), which results in a maximum that gradually decays to a steady state as the fault slip velocity reaches the background loading rate (Figure 18).

5. Summary

We report on a laboratory study of the effect of normal stress perturbations on the evolution of friction and fault strength. Our observations include applied stresses, frictional strength, and elastic properties determined from ultrasonic waves transmitted across the fault during step increases in normal stress. We find that shear stress evolution in response to an imposed increase in normal stress is adequately described by the Linker and Dieterich (1992) formulation within the RSF framework. Additionally, we find that contrasting observations of shear stress evolution reported in previous works can be resolved by accounting for loading stiffness and changes in slip rate associated with changes in normal stress.

We show that elastic wave amplitude is a reliable proxy for frictional state and the real area of surface contact at steady state. Our results indicate a complex interaction between time and slip in the evolution of wave amplitude in response to changes in fault normal stress. Specifically, we find evidence for a time-dependent increase in amplitude that is well correlated with the elastic phase of shear stress increase after a normal stress increase, which is consistent with fault locking. However, the best fit numerical simulations to our experimental data indicate that frictional state does not increase in this manner, and instead only increases as the fault accelerates to the background sliding rate. We reconcile these observations by considering state as embodying some measure of the contact scale area as well as shear resistance. While the idea that frictional state is a combination of contact area and quality is not new, our work provides new insights for the application of this theory to normal stress changes. Future work could explore the possibility that our observations may also be reconciled by using a combination of slip and time-dependent state evolution laws.

We test our assumption regarding the use of ultrasonic P wave amplitude as a proxy for contact area and find that not only does P wave amplitude increase linearly with normal stress, but it can also be used to
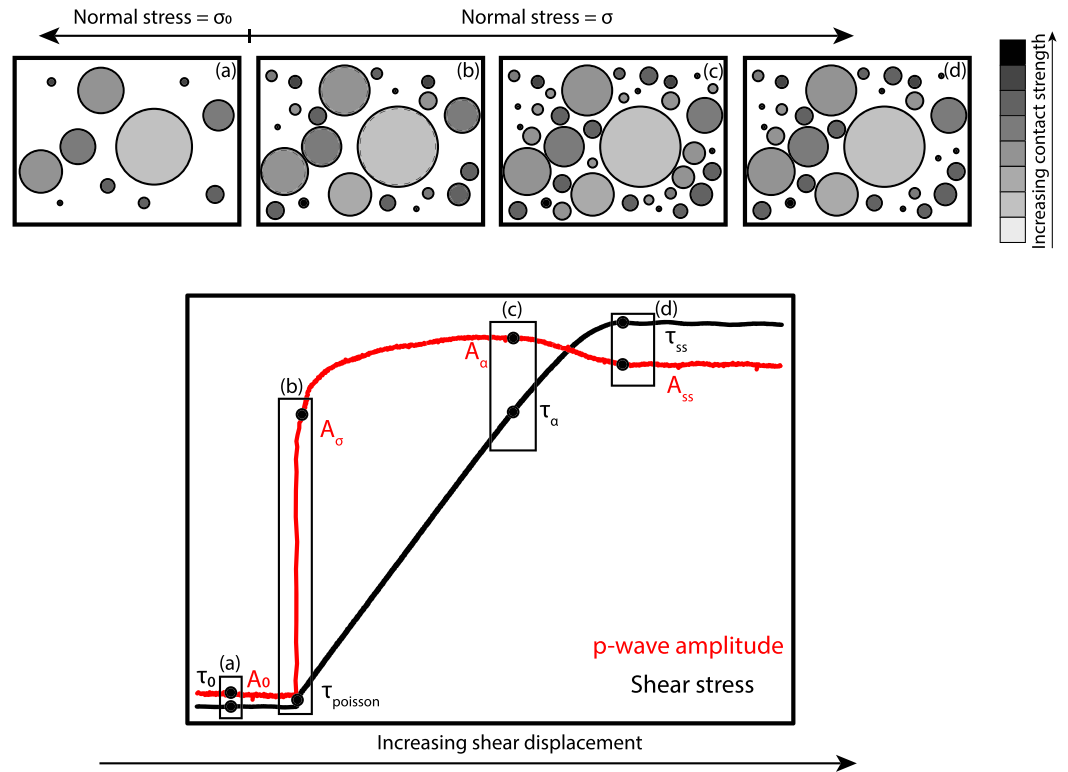
Figure 18. Schematic to illustrate contact scale mechanisms that govern shear stress and wave amplitude during a normal stress step. Images show plan view of a friction surface with Hertzian contact junctions with a range of sizes and strengths (grey scale). (a) Initial contact distribution at baseline normal stress. (b) Contact area increases instantaneously as normal stress is increased, by both increased size of existing asperities and the creation of new asperities such that average asperity size remains unchanged; (c) contact area continues to increase during elastic loading due to aging and the drop in slip rate; (d) as slip rate increases back to the initial value, contacts are rejuvenated by slip with weaker, younger contacts being preferentially destroyed, and wave amplitude decreases to a steady state corresponding to the new normal stress.

independently constrain the state parameter α. Based on these observations, we use the variations in amplitude to propose a microphysical model for contact-scale behavior during rapid normal stress perturbations. Our results illustrate the importance of accounting for changes in frictional strength, in addition to applied stresses, in earthquake triggering by static and dynamic stresses. Future work focusing on more general forms of dynamic stressing and more complex conditions, of pore fluid pressure and temperature, will be useful to better understand the effect of normal stress perturbations on fault friction.

Appendix A: Relation Between Ultrasonic Amplitude and Transmission Coefficient

Considering a single granite block of thickness t with an attenuation coefficient γ, the transmitted A_0 is given by:

$$A_0 = A_I e^{-\gamma t} \tag{A1}$$

where A_I represents the incident elastic wave amplitude. Here we assume that this granite block has a thickness equivalent to the combined thicknesses of the three granite blocks in the DDS assembly, that is, $t = t_1 + t_2 + t_3$. Now considering three granite blocks and therefore two interfaces, the transmitted amplitude (denoted A_T) in this case becomes

$$A_T = T^2 A_I e^{-\gamma t_1 - \gamma t_2 - \gamma t_3} = T^2 A_I e^{-\gamma t} \tag{A2}$$

where T represents the transmission coefficient of a single interface. Now dividing equation (A2) by equation (A1), we obtain

$$A_T = T^2 A_0 \tag{A3}$$

Again, A_0 is the transmitted amplitude across a single granite block in the case where no interface is present. The amplitude A reported in the manuscript—taken as the square root of A_T—is proportional to the transmission coefficient across a single interface:

$$A = \sqrt{A_T} = T\sqrt{A_0} \tag{A4}$$

$$A \propto T \tag{A5}$$

References

Andrews, D. J., & Ben-Zion, Y. (1997). Wrinkle-like slip pulse on a fault between different materials. *Journal of Geophysical Research*, *102*(B1), 553–571. https://doi.org/10.1029/96JB02856

Bayart, E., Rubin, A. M., & Marone, C. (2006, December). Evolution of fault friction following large velocity jumps. In AGU Fall Meeting Abstracts.

Beeler, N. M., Tullis, T. E., & Weeks, J. D. (1994). The roles of time and displacement in the evolution effect in rock friction. *Geophysical Research Letters*, *21*(18), 1987–1990. https://doi.org/10.1029/94GL01599

Bhat, H. S., Dmowska, R., Rice, J. R., & Kame, N. (2004). Dynamic slip transfer from the Denali to Totschunda faults, Alaska: Testing theory for fault branching. *Bulletin of the Seismological Society of America*, *94*(6B), S202–S213. https://doi.org/10.1785/0120040601

Bhattacharya, P. (2017). Examination of the rate-state friction equations under large perturbations from steady sliding: A theoretical and experimental study (Doctoral dissertation, Princeton University).

Bhattacharya, P., Rubin, A. M., Bayart, E., Savage, H. M., & Marone, C. (2015). Critical evaluation of state evolution laws in rate and state friction: Fitting large velocity steps in simulated fault gouge with time-, slip-, and stress-dependent constitutive laws. *Journal of Geophysical Research: Solid Earth*, *120*, 6365–6385. https://doi.org/10.1002/2015JB012437

Bhattacharya, P., Rubin, A. M., & Beeler, N. M. (2017). Does fault strengthening in laboratory rock friction experiments really depend primarily upon time and not slip? *Journal of Geophysical Research: Solid Earth*, *122*, 6389–6430. https://doi.org/10.1002/2017JB013936

Biegel, R. L., Wang, W., Scholz, C. H., Boitnott, G. N., & Yoshioka, N. (1992). Micromechanics of rock friction 1. Effects of surface roughness on initial friction and slip hardening in westerly granite. *Journal of Geophysical Research*, *97*(B6), 8951–8964. https://doi.org/10.1029/92JB00042

Boettcher, M. S., & Marone, C. J. (2004). Effects of normal stress variation on the strength and stability of creeping faults. *Journal of Geophysical Research*, *109*, B03406. https://doi.org/10.1029/2003JB002824

Bowden, F. P., & Tabor, D. (1951). The friction and lubrication of solids. *American Journal of Physics*, *19*(7), 428–429. https://doi.org/10.1119/1.1933017

Brodsky, E. E., Kirkpatrick, J. D., & Candela, T. (2016). Constraints from fault roughness on the scale-dependent strength of rocks. *Geology*, *44*(1), 19–22. https://doi.org/10.1130/G37206.1

Bureau, L., Baumberger, T., & Caroli, C. (2002). Rheological aging and rejuvenation in solid friction contacts. *The European Physical Journal E*, *8*(3), 331–337. https://doi.org/10.1140/epje/i2002-10017-1

Byerlee, J. D. (1967). Frictional characteristics of granite under high confining pressure. *Journal of Geophysical Research*, *72*(14), 3639–3648. https://doi.org/10.1029/JZ072i014p03639

Cochard, A., & Rice, J. R. (2000). Fault rupture between dissimilar materials: Ill-posedness, regularization, and slip-pulse response. *Journal of Geophysical Research*, *105*(B11), 25,891–25,907. https://doi.org/10.1029/2000JB900230

Delorey, A. A., van der Elst, N. J., & Johnson, P. A. (2017). Tidal triggering of earthquakes suggests poroelastic behavior on the San Andreas Fault. *Earth and Planetary Science Letters*, *460*, 164–170. https://doi.org/10.1016/j.epsl.2016.12.014

Dieterich, J. H. (1979). Modeling of rock friction: 1. Experimental results and constitutive equations. *Journal of Geophysical Research*, *84*(B5), 2161–2168. https://doi.org/10.1029/JB084iB05p02161

Dieterich, J. H., & Conrad, G. (1984). Effect of humidity on time-and velocity-dependent friction in rocks. *Journal of Geophysical Research*, *89*(B6), 4196–4202. https://doi.org/10.1029/JB089iB06p04196

Dieterich, J. H., & Kilgore, B. D. (1994). Direct observation of frictional contacts: New insights for state-dependent properties. *Pure and Applied Geophysics*, *143*(1-3), 283–302. https://doi.org/10.1007/BF00874332

Dunham, E. M., Belanger, D., Cong, L., & Kozdon, J. E. (2011). Earthquake ruptures with strongly rate-weakening friction and off-fault plasticity. Part 2: Nonplanar faults. *Bulletin of the Seismological Society of America*, *101*(5), 2308–2322. https://doi.org/10.1785/0120100076

Fan, W., & Shearer, P. M. (2016). Local near instantaneously dynamically triggered aftershocks of large earthquakes. *Science*, *353*(6304), 1133–1136. https://doi.org/10.1126/science.aag0013

Fang, Z., Dieterich, J. H., Richards-Dinger, K. B., & Xu, G. (2011). Earthquake nucleation on faults with nonconstant normal stress. *Journal of Geophysical Research*, *116*, B09307. https://doi.org/10.1029/2011JB008196

Freed, A. M. (2005). Earthquake triggering by static, dynamic, and postseismic stress transfer. *Annual Review of Earth and Planetary Sciences*, *33*(1), 335–367. https://doi.org/10.1146/annurev.Earth.33.092203.122505

Frye, K. M., & Marone, C. (2002). Effect of humidity on granular friction at room temperature. *Journal of Geophysical Research*, *107*(B11), 2309. https://doi.org/10.1029/2001JB000654

Goebel, T. H., & Brodsky, E. E. (2018). The spatial footprint of injection wells in a global compilation of induced earthquake sequences. *Science*, *361*(6405), 899–904. https://doi.org/10.1126/science.aat5449

Gomberg, J., Beeler, N. M., Blanpied, M. L., & Bodin, P. (1998). Earthquake triggering by transient and static deformations. *Journal of Geophysical Research*, *103*(B10), 24,411–24,426. https://doi.org/10.1029/98JB01125

Gomberg, J., & Johnson, P. A. (2005). Dynamic triggering of earthquakes. *Nature*, *437*(7060), 830. https://doi.org/10.1038/nature04167

Greenwood, J. A., & Williamson, J. P. (1966). Contact of nominally flat surfaces. *Proceedings of the Royal Society of London A*, *295*(1442), 300–319. https://doi.org/10.1098/rspa.1966.0242

Haimson, B., & Chang, C. (2000). A new true triaxial cell for testing mechanical properties of rock, and its use to determine rock strength and deformability of westerly granite. *International Journal of Rock Mechanics and Mining Sciences*, *37*(1-2), 285–296. https://doi.org/10.1016/S1365-1609(99)00106-9

Harris, R. A. (1998). Introduction to special section: Stress triggers, stress shadows, and implications for seismic hazard. *Journal of Geophysical Research*, *103*(B10), 24,347–24,358. https://doi.org/10.1029/98JB01576

Harris, R. A., & Simpson, R. W. (1992). Changes in static stress on southern California faults after the 1992 Landers earthquake. *Nature*, *360*(6401), 251–254. https://doi.org/10.1038/360251a0

He, C., & Wong, T. F. (2014). Effect of varying normal stress on stability and dynamic motion of a spring-slider system with rate-and state-dependent friction. *Earthquake Science*, *27*(6), 577–587. https://doi.org/10.1007/s11589-014-0098-4

Hill, D. P., Reasenberg, P. A., Michael, A., Arabaz, W. J., Beroza, G., Brumbaugh, D., et al. (1993). Seismicity remotely triggered by the magnitude 7.3 Landers, California, Earthquake. *Science*, *260*(5114), 1617–1623. https://doi.org/10.1126/science.260.5114.1617

Hobbs, B. E., & Brady, B. H. G. (1985). Normal stress changes and the constitutive law for rock friction. EOS. Transactions of the American Geophysical Union, 66, 382.

Hong, T., & Marone, C. J. (2005). Effects of normal stress perturbations on the frictional properties of simulated faults. *Geochemistry, Geophysics, Geosystems*, *6*, Q03012. https://doi.org/10.1029/2004GC000821

Ikari, M. J., Carpenter, B. M., & Marone, C. (2016). A microphysical interpretation of rate-and state-dependent friction for fault gouge. *Geochemistry, Geophysics, Geosystems*, *17*, 1660–1677. https://doi.org/10.1002/2016GC006286

Itaba, S., & Ando, R. (2011). A slow slip event triggered by teleseismic surface waves. *Geophysical Research Letters*, *38*, L21306. https://doi.org/10.1029/2011GL049593

Johnson, C. W., Bürgmann, R., & Pollitz, F. F. (2015). Rare dynamic triggering of remote M ≥ 5.5 earthquakes from global catalog analysis. *Journal of Geophysical Research: Solid Earth*, *120*, 1748–1761. https://doi.org/10.1002/2014JB011788

Kendall, K., & Tabor, D. (1971). An ultrasonic study of the area of contact between stationary and sliding surfaces. *Proceedings of the Royal Society of London A*, *323*(1554), 321–340. https://doi.org/10.1098/rspa.1971.0108

Kilb, D., Gomberg, J., & Bodin, P. (2000). Triggering of earthquake aftershocks by dynamic stresses. *Nature*, *408*(6812), 570–574. https://doi.org/10.1038/35046046

Kilgore, B., Beeler, N. M., Lozos, J., & Oglesby, D. (2017). Rock friction under variable normal stress. *Journal of Geophysical Research: Solid Earth*, *122*, 7042–7075. https://doi.org/10.1002/2017JB014049

Kilgore, B., Lozos, J., Beeler, N., & Oglesby, D. (2012). Laboratory observations of fault strength in response to changes in normal stress. *Journal of Applied Mechanics*, *79*(3), 031007. https://doi.org/10.1115/1.4005883

King, G. C. P., Stein, R. S., & Lin, J. (1994). Static stress changes and the triggering of earthquakes. *Bulletin of the Seismological Society of America*, *32*(2), A50–A51. https://doi.org/10.1016/0148-9062(95)94484-2

Leeman, J., Scuderi, M. M., Marone, C., & Saffer, D. (2015). Stiffness evolution of granular layers and the origin of repetitive, slow, stick-slip frictional sliding. *Granular Matter*, *17*(4), 447–457. https://doi.org/10.1007/s10035-015-0565-1

Leeman, J. R., Marone, C., & Saffer, D. M. (2018). Frictional mechanics of slow earthquakes. *Journal of Geophysical Research: Solid Earth*, *123*, 7931–7949. https://doi.org/10.1029/2018JB015768

Leeman, J. R., Saffer, D. M., Scuderi, M. M., & Marone, C. (2016). Laboratory observations of slow earthquakes and the spectrum of tectonic fault slip modes. *Nature Communications*, *7*(1), 11104. https://doi.org/10.1038/ncomms11104

Li, Q., Tullis, T. E., Goldsby, D., & Carpick, R. W. (2011). Frictional ageing from interfacial bonding and the origins of rate and state friction. *Nature*, *480*(7376), 233–236. https://doi.org/10.1038/nature10589

Li, T., & Rubin, A. M. (2017). A microscopic model of rate and state friction evolution. *Journal of Geophysical Research: Solid Earth*, *122*, 6431–6453. https://doi.org/10.1002/2017JB013970

Linker, M. F., & Dieterich, J. H. (1992). Effects of variable normal stress on rock friction: Observations and constitutive equations. *Journal of Geophysical Research*, *97*(B4), 4923. https://doi.org/10.1029/92JB00017

Ma, S., & Beroza, G. C. (2008). Rupture dynamics on a bimaterial interface for dipping faults. *Bulletin of the Seismological Society of America*, *98*(4), 1642–1658. https://doi.org/10.1785/0120070201

Mair, K., & Marone, C. (1999). Friction of simulated fault gouge for a wide range of velocities and normal stresses. *Journal of Geophysical Research*, *104*(B12), 28,899–28,914. https://doi.org/10.1029/1999JB900279

Manga, M., & Brodsky, E. (2006). Seismic triggering of eruptions in the far field: Volcanoes and Geysers. *Annual Review of Earth and Planetary Sciences*, *34*(1), 263–291. https://doi.org/10.1146/annurev.earth.34.031405.125125

Marone, C. (1998a). The effect of loading rate on static friction and the rate of fault healing during the earthquake cycle. *Nature*, *391*(6662), 69–72. https://doi.org/10.1038/34157

Marone, C. (1998b). Laboratory-derived friction laws and their application to seismic faulting. *Annual Review of Earth and Planetary Sciences*, *26*(1), 643–696. https://doi.org/10.1146/annurev.earth.26.1.643

Marone, C., & Kilgore, B. (1993). Scaling of the critical slip distance for seismic faulting with shear strain in fault zones. *Nature*, *362*(6421), 618–621. https://doi.org/10.1038/362618a0

Molinari, A., & Perfettini, H. (2017). A micromechanical model of rate and state friction: 2. Effect of shear and normal stress changes. *Journal of Geophysical Research: Solid Earth*, *122*, 2638–2652. https://doi.org/10.1002/2016JB013307

Nagata, K., Kilgore, B., Beeler, N., & Nakatani, M. (2014). High-frequency imaging of elastic contrast and contact area with implications for naturally observed changes in fault properties. *Journal of Geophysical Research: Solid Earth*, *119*, 5855–5875. https://doi.org/10.1002/2014JB011014

Nagata, K., Nakatani, M., & Yoshida, S. (2008). Monitoring frictional strength with acoustic wave transmission. *Geophysical Research Letters*, *35*, L06310. https://doi.org/10.1029/2007GL033146

Nagata, K., Nakatani, M., & Yoshida, S. (2012). A revised rate- and state-dependent friction law obtained by constraining constitutive and evolution laws separately with laboratory data. *Journal of Geophysical Research*, *117*, B02314. https://doi.org/10.1029/2011JB008818

Niemeijer, A. R., & Spiers, C. J. (2006). Velocity dependence of strength and healing behaviour in simulated phyllosilicate-bearing fault gouge. *Tectonophysics*, *427*(1-4), 231–253. https://doi.org/10.1016/j.tecto.2006.03.048

Olsson, W. A. (1988, January). The effects of normal stress history on rock friction. In The 29th US Symposium on Rock Mechanics (USRMS). American Rock Mechanics Association.

Peng, Z., & Gomberg, J. (2010). An integrated perspective of the continuum between earthquakes and slow-slip phenomena. *Nature Geoscience*, *3*(9), 599–607. https://doi.org/10.1038/ngeo940

Prakash, V. (1998). Frictional response of sliding interfaces subjected to time varying normal pressures. *Journal of Tribology*, *120*(1), 97. https://doi.org/10.1115/1.2834197

Prakash, V., & Clifton, R. J. (1993). Time resolved dynamic friction measurements in pressure-shear. *ASME Applied Mechanics Division-publications-AMD*, *165*, 33–33.

Press, W. H., Teukolsky, S. A., Vetterling, W. T., & Flannery, B. P. (1992). *Numerical recipies in C* (Vol. 2). Cambridge: Cambridge University Press.

Pyrak-Nolte, L. J., Myer, L. R., & Cook, N. G. (1990). Transmission of seismic waves across single natural fractures. *Journal of Geophysical Research*, *95*(B6), 8617–8638. https://doi.org/10.1029/JB095iB06p08617

Rabinowicz, E. (1951). The nature of the static and kinetic coefficients of friction. *Journal of Applied Physics*, *22*(11), 1373–1379. https://doi.org/10.1063/1.1699869

Rabinowicz, E. (1956). Stick and slip. *Scientific American*, *194*(5), 109–119. Retrieved from. http://www.jstor.org/stable/26122743, https://doi.org/10.1038/scientificamerican0556-109

Raleigh, C. B., Healy, J. H., & Bredehoeft, J. D. (1976). An experiment in earthquake control at Rangely, Colorado. *Science*, *191*(4233), 1230–1237. https://doi.org/10.1126/science.191.4233.1230

Ranjith, K., & Rice, J. R. (2001). Slip dynamics at an interface between dissimilar materials. *Journal of the Mechanics and Physics of Solids*, *49*(2), 341–361. https://doi.org/10.1016/S0022-5096(00)00029-6

Renard, F., Beauprêtre, S., Voisin, C., Zigone, D., Candela, T., Dysthe, D. K., & Gratier, J. P. (2012). Strength evolution of a reactive frictional interface is controlled by the dynamics of contacts and chemical effects. *Earth and Planetary Science Letters*, *341-344*, 20–34. https://doi.org/10.1016/j.epsl.2012.04.048

Richardson, E., & Marone, C. J. (1999). Effects of normal stress vibrations on frictional healing. *Journal of Geophysical Research*, *104*(B12), 28,859–28,878. https://doi.org/10.1029/1999JB900320

Rivière, J., Lv, Z., Johnson, P. A., & Marone, C. (2018). Evolution of b -value during the seismic cycle: Insights from laboratory experiments on simulated faults. *Earth and Planetary Science Letters*, *482*, 407–413. https://doi.org/10.1016/j.epsl.2017.11.036

Rubinstein, J. L., La Rocca, M., Vidale, J. E., Creager, K. C., & Wech, A. G. (2008). Tidal modulation of nonvolcanic tremor. *Science*, *319*(5860), 186–189. https://doi.org/10.1126/science.1150558

Ruina, A. (1983). Slip instability and state variable friction laws. *Journal of Geophysical Research*, *88*(B12), 10,359–10,370. https://doi.org/10.1029/JB088iB12p10359

Saffer, D. M., & Marone, C. (2003). Comparison of smectite-and illite-rich gouge frictional properties: application to the updip limit of the seismogenic zone along subduction megathrusts. *Earth and Planetary Science Letters*, *215*(1-2), 219–235. https://doi.org/10.1016/S0012-821X(03)00424-2

Scholz, C. H. (2002). *The mechanics of earthquakes and faulting*. Cambridge: Cambridge university press. https://doi.org/10.1017/CBO9780511818516

Scuderi, M. M., Carpenter, B. M., & Marone, C. (2014). Physicochemical processes of frictional healing: Effects of water on stick-slip stress drop and friction of granular fault gouge. *Journal of Geophysical Research: Solid Earth*, *119*, 4090–4105. https://doi.org/10.1002/2013JB010641

Scuderi, M. M., Collettini, C., Viti, C., Tinti, E., & Marone, C. (2017). Evolution of shear fabric in granular fault gouge from stable sliding to stick slip and implications for fault slip mode. *Geology*, *45*(8), G39033.1–G39033.734. https://doi.org/10.1130/G39033.1

Scuderi, M. M., Marone, C., Tinti, E., Di Stefano, G., & Collettini, C. (2016). Precursory changes in seismic velocity for the spectrum of earthquake failure modes. *Nature Geoscience*, *9*(9), 695–700. https://doi.org/10.1038/ngeo2775

Sharp, T. A., Pastewka, L., Lignères, V. L., & Robbins, M. O. (2017). Scale-and load-dependent friction in commensurate sphere-on-flat contacts. *Physical Review B*, *96*(15), 155436. https://doi.org/10.1103/PhysRevB.96.155436

Solberg, P., & Byerlee, J. D. (1984). A note on the rate sensitivity of frictional sliding of Westerly granite. *Journal of Geophysical Research*, *89*(B6), 4203–4205.

Tan, Y. J., Tolstoy, M., Waldhauser, F., & Bohnenstiehl, D. R. (2018). Tidal Triggering of Microearthquakes Over an Eruption Cycle at 9°50′ N East Pacific Rise. *Geophysical Research Letters*, *45*, 1825–1831. https://doi.org/10.1002/2017GL076497

Tanaka, K., Moriyama, R., & Miki, I. (2006). Initial rotor position estimation of interior permanent magnet synchronous motor using optimal voltage vector. *Electrical Engineering in Japan*, *156*(4), 69–76. https://doi.org/10.1002/eej.20062

Thom, C. A., Brodsky, E. E., Carpick, R. W., Pharr, G. M., Oliver, W. C., & Goldsby, D. L. (2017). Nanoscale roughness of natural fault surfaces controlled by scale-dependent yield strength. *Geophysical Research Letters*, *44*, 9299–9307. https://doi.org/10.1002/2017GL074663

Tian, K., Gosvami, N. N., Goldsby, D. L., & Carpick, R. W. (2017). Stick–slip instabilities for interfacial chemical bond-induced friction at the nanoscale. *The Journal of Physical Chemistry B*, *122*(2), 991–999. https://doi.org/10.1021/acs.jpcb.7b09748

Tullis, J., & Yund, R. A. (1977). Experimental deformation of dry westerly granite. *Journal of Geophysical Research*, *82*(36), 5705–5718. https://doi.org/10.1029/JB082i036p05705

Tullis, T. E., & Weeks, J. D. (1986). Constitutive behavior and stability of frictional sliding of granite. *Pure and Applied Geophysics*, *124*(3), 383–414. https://doi.org/10.1007/BF00877209

Van der Elst, N. J., Savage, H. M., Keranen, K. M., & Abers, G. A. (2013). Enhanced remote earthquake triggering at fluid-injection sites in the midwestern United States. *Science*, *341*(6142), 164–167. https://doi.org/10.1126/science.1238948

Wallace, L. M., Kaneko, Y., Hreinsdóttir, S., Hamling, I., Peng, Z., Bartlow, N., et al. (2017). Large-scale dynamic triggering of shallow slow slip enhanced by overlying sedimentary wedge. *Nature Geoscience*, *10*(10), 765–770. https://doi.org/10.1038/ngeo3021

Wesnousky, S. G. (2006). Predicting the endpoints of earthquake ruptures. *Nature*, *444*(7117), 358–360. https://doi.org/10.1038/nature05275

Wong, T. F. (1982). Micromechanics of faulting in westerly granite. In *International journal of rock mechanics and mining sciences & geomechanics abstracts*, (Vol. 19, No. 2, pp. 49–64). Pergamon Press, Pergamon. https://doi.org/10.1016/0148-9062(82)91631-X

Yoshioka, N., & Iwasa, K. (1996). The characteristic displacement in rate and state-dependent friction from a micromechanical point of view. *Pure and Applied Geophysics*, *147*(3), 433–453. https://doi.org/10.1007/BF00878837

Yoshioka, N., & Iwasa, K. (2006). A laboratory experiment to monitor the contact state of a fault by transmission waves. *Tectonophysics*, *413*(3-4), 221–238. https://doi.org/10.1016/j.tecto.2005.10.035